Remote Sensing of Environment 272 (2022) 112906

Contents lists available at ScienceDirect

Remote Sensing of Environment

journal homepage: www.elsevier.com/locate/rse

New insights into the Asian dust cycle derived from CALIPSO lidar measurements

Ying Han [a], Tianhe Wang [a,b,*], Jingyi Tang [a], Chengyun Wang [a], Bida Jian [a], Zhongwei Huang [a,b], Jianping Huang [a,b]

[a] Key Laboratory for Semi-Arid Climate Change of the Ministry of Education, College of Atmospheric Sciences, Lanzhou University, Lanzhou 730000, China
[b] Collaborative Innovation Center for Western Ecological Safety, Lanzhou University, Lanzhou 730000, China

ARTICLE INFO

Editor: Menghua Wang

Keywords:
Asian dust
Dust mass loading
Transport central axis
Transport flux
Desert-source contribution

ABSTRACT

A full understanding of the Asian dust cycle can help with evaluation of the profound impact of mineral dust on human health, the ecosystem, the terrestrial and oceanic biogeochemical cycles, and the weather and climate. The Cloud-Aerosol Lidar with Orthogonal Polarization (CALIOP)-based 3-D dust detection and routine sampling capability, with the accurate dust mass extinction efficiency from Dust Constraints from joint Observational-Modelling-experimental analysis (DustCOMM) dataset, has made it possible to estimate the climatology of Asian dust mass loading (DML) and its transport flux. This study draws on this to provide new insights into the Asian dust cycle, especially the variability of its mass-weighted dust transport central axis (TCA), the contribution of different desert sources to its downstream effects, and the resulting dust budgets in terrestrial and oceanic regions. Dust aerosols emitted from the East Asian and Central Asian deserts together form a heavy dust transport belt stretching from the Taklimakan Desert (TD) and Gobi Desert (GD) to the Pacific Ocean. South Asian dust from the Thar Desert (ThD) can also affect southern China by crossing the Hengduan Mountains and the Yunnan-Guizhou Plateau. The dust TCA is controlled by the terrain of northwest inland China, but shifts in remote regions in the range of 35-50°N due to the western Pacific subtropical high and Aleutian low, and it trend towards a zonal straight line as the altitude increases. The dust transport contribution of the East Asian deserts to the mainland of China and adjacent sea is about 7 times than that of South Asia, with the annual transport fluxes being 214.28 and 30.43 Tg, respectively. The GD dominates the contribution of Asian deserts to the downstream effects and accounts for about 60% of the dust. This can be attributed to its maximum transport flux being near the surface, while the dust transport of the TD and ThD is above 3 km because of the blocking effect of the surrounding terrain. The deposition of Asian dust in the adjacent seas decreases significantly along the dust TCA, with the annual deposition rates being about 40.12, 20.41, and 4.01 g m^{-2} in the Yellow Sea, Japan Sea and the Northwest Pacific Ocean, respectively. These new findings and quantification of the Asian dust cycle will help with validation of the simulations provided by global and regional climate models and enable further evaluation of the impact of Asian dust on various related Earth systems.

1. Introduction

Asia is the second-largest dust source in the world after Africa, resulting from the extensive deserts distributed across Kazakhstan, northwest China, Mongolia and India. A large amount of the dust from these deserts is ejected into the atmosphere and transported to downstream areas. The direct, semi-direct and indirect effects of this dust can modulate the radiation budget of the earth-atmosphere system (Huang et al., 2014; Paulot et al., 2018) and affect regional and global weather and climate (Kaufman et al., 2002; Kudo et al., 2016). It has been proved that dust from South Asia can be lifted and transported over the Tibetan Plateau (TP) (Lau et al., 2006; Wang et al., 2021b), potentially accelerating the decline of glaciers (Lau et al., 2018; Usha et al., 2021; Wang et al., 2020a). Approximately 600 Tg of East Asian dust, mainly emitted from the Taklimakan Desert (TD) and Gobi Desert (GD), is released into the atmosphere annually (Zhang et al., 1997). This dust can sweep

* Corresponding author at: Key Laboratory for Semi-Arid Climate Change of the Ministry of Education, College of Atmospheric Sciences, Lanzhou University, Lanzhou 730000, China.
E-mail address: wangth@lzu.edu.cn (T. Wang).

https://doi.org/10.1016/j.rse.2022.112906
Received 12 August 2021; Received in revised form 24 December 2021; Accepted 11 January 2022
Available online 3 February 2022

across the whole of northern China (Ginoux and Deroubaix, 2017; Yu et al., 2019b) and a large portion of eastern China (Zhang et al., 2005), Korea and Japan (Kim et al., 2010; Yu et al., 2020), before being deposited into the Pacific (Huang et al., 2008; Kim et al., 2019). It can even be transported to the west of America (Guo et al., 2017; Schuerger et al., 2018; Uno et al., 2011; Yu et al., 2012). As a result, large quantities of microelements can be carried by the dust aerosols and deposited into the ocean, making it an important part of the terrestrial and oceanic biogeochemical cycle (Maki et al., 2021; Prospero et al., 2020). This has led to the connections between the Asian dust cycle, biogeochemical cycles and the global climate becoming a core theme in Earth system science (Shao et al., 2011). Accurate assessment of the dust cycle process (e.g., dust emission, transport and deposition) over Asia is of key scientific concern.

To date, model simulations and reanalysis datasets have been widely used to depict the dust cycle over Asia. These provide valuable information at a mechanistic level, shedding light on dust phenomena and their detailed physical processes at a regional and global scale and improving our understanding of dust-related processes and the effects of dust on the environment and climate (Shao and Dong, 2006; Uno et al., 2006). Chen et al. (2017a) investigated the contribution of the TD and GD to the dust loading of East Asia by drawing upon the Weather Research and Forecasting model coupled with Chemistry (WRF-Chem). The study found that the TD has the highest dust emission capability - about 70.54 Tg yr^{-1} in the spring - but makes a smaller contribution to the dust loading of East Asia than the GD. Liu et al. (2015) used the Spectral Radiation-Transport Model for Aerosol Species (SPRINTARS) with a non-hydrostatic regional model (NHM) to prove that anthropogenic aerosols from South Asia transport to the southern slopes of the TP via southwesterly winds. This is consistent with the results of Sun et al. (2020), which are based on the Second Modern-Era Retrospective analysis for Research and Applications (MERRA-2). However, large uncertainties exist in the simulated results due to differences in dust emission parameterization schemes, deposition schemes, meteorological conditions, underlying surface effects, and so on (Huneeus et al., 2011; Sicard et al., 2021; Uno et al., 2009). Independent and effective observation of the dust cycle is therefore the most powerful way to evaluate, constrain, and improve existing model simulations (Chen et al., 2017b; Klose et al., 2014).

The recent boom in satellite-based observations has provided ideal tools for studying the global distribution of dust aerosols because of their large spatial and temporal coverage (Ginoux and Deroubaix, 2017). Previous studies have used satellite observations of dust-related phenomena and its optical properties to expose a number of important aspects of the dust cycle process over Asia (Cheng et al., 2020; Lakshmi et al., 2021; Song et al., 2021; Toth et al., 2016). For example, Proestakis et al. (2018) used the seasonal dust event frequency, dust optical depth (DOD), and particulate depolarization ratio (PDR) captured by the Cloud-Aerosol Lidar with Orthogonal Polarization (CALIOP) to reveal the high dust emissions from the deserts in South Asia and East Asia and their potential transport variation. Kim et al. (2019) described the seasonal and vertical distribution of dust aerosols over Asia and the North Pacific by using the DOD provided by multiple satellite and ground-based measurements, thereby revealing the longitudinal gradient during the trans-Pacific transport. Song et al. (2021) also analyzed dust records from CALIOP and the Moderate Resolution Imaging Spectroradiometer (MODIS) and found a decreasing trend of dust from the Gobi Desert (associated with increased vegetation cover) and over the Northwest Pacific Ocean (NPO). However, for a more comprehensive understanding of dust transport, researchers need to use the satellite observed DOD to acquire more accurate dust mass loading measurements (Kaufman et al., 2005). They will then be able to better depict the actual amount of dust mass in the atmosphere (Xu et al., 2018) and its deposition into the oceans (Maki et al., 2021). This will improve the forecasting capacity of regional and global simulation models (Shi et al., 2020).

The factor used to convert DOD to dust mass concentration (DMC) is the dust mass extinction efficiency (MEE) (Kim et al., 2019). This changes according to variations in the physical and chemical properties of dust aerosols (Denjean et al., 2020; Ginoux et al., 2012). However, due to the limitations of existing satellite remote sensing technology, it is fiendishly hard to directly derive real-time dust MEE. To address this issue, most studies tend to treat it as either a fixed constant of 0.37 $m^2 g^{-1}$ (Yu et al., 2015a), 0.6 $m^2 g^{-1}$ (Huang et al., 2015), or a linearly-varying function (Yu et al., 2019a). Unfortunately, this can introduce a large amount of uncertainty in DMC inversion algorithms (Müller et al., 2010). The assumption of a dust MEE of 0.37 (0.60) $m^2 g^{-1}$ can overestimate (or underestimate) the DMC by about 20–40% (15–30%) in northwestern China (Wang et al., 2021a). Although effort has been devoted to acquiring a dust MEE based on joint lidar and sun-photometer observations (Ansmann et al., 2019; Ansmann et al., 2011; Wang et al., 2021a), it is difficult to obtain a spatially and temporally continuous dust MEE because of the non-uniform distribution of the acquisition sites. Fortunately, a new Dust Constraints from joint Observational-Modelling-experimental analysis (DustCOMM) dataset has recently been developed by Adebiyi et al. (2020). This can provide the 3-D size distribution of dust aerosols by using multiple satellites and global AERONET products and by coupling six leading atmospheric global models, and further obtain a well-contrained dust MEE at a global scale. So, it has now become possible to accurately evaluate the regional and global dust cycle.

In this study, the accurate 3-D dust detection from CALIOP and dust MEE from the DustCOMM dataset have been used to estimate the 3-D total dust mass loading (DML) and dust mass transport flux rate (DFR) over Asia from 2007 to 2018. This contains both natural and anthropogenic dust extracted from dust-containing aerosol types, e.g., polluted dust and dusty marine. The DML results were evaluated and compared with those provided by the MERRA-2 and DustCOMM datasets. The seasonal 3-D evolution of Asian dust along mass-weighted transport central axis (TCA) was then characterized. In view of the limitations of satellite observation, it is hard to acquire the dust emission mass over source areas directly. However, it was possible to use the DFR to quantitatively evaluate the downstream contribution of three dust sources (S1-S3) and the dust budget of five transport regions along the dust TCA (see Fig. 1). This study offers new insights into the Asian dust cycle using satellite observations and can provide effective support for related research based using model simulations.

2. Datasets and methodology

2.1. DustCOMM dataset

Obtaining accurate constraints regarding the wide variety of impacts dust can have on Earth systems requires accurate knowledge of the size, abundance, and optical properties of atmospheric dust particles (Mahowald et al., 2014). Global model simulations of the dust cycle can therefore be subject to the numerous important biases from these above properties. To address the problem of size and shape bias in simulations of dust properties, Adebiyi et al. (2020) developed the DustCOMM dataset. This combines an ensemble of six global simulations with observational and experimental constraints relating to dust size distribution and shape. DustCOMM offers more accurate atmospheric dust properties than independent measurements and other model ensembles (Adebiyi et al., 2020; Kok et al., 2017). The dust properties include an annual and seasonal climatology of 3-D dust size distribution, the 2-D dust MEE at 550 nm, and atmospheric dust loading. The DustCOMM MEE makes a negligible difference (~1%) relative to other measurements of MEE (Adebiyi et al., 2020; Kok et al., 2017). This dataset not only helps to improve the accuracy of the impact of dust in earth system simulations, but also assists in the evaluation of the climatology of DML-based satellite observations by providing an accurate dust MEE, as will be seen below. Here, the seasonal dust MEE climatology with a

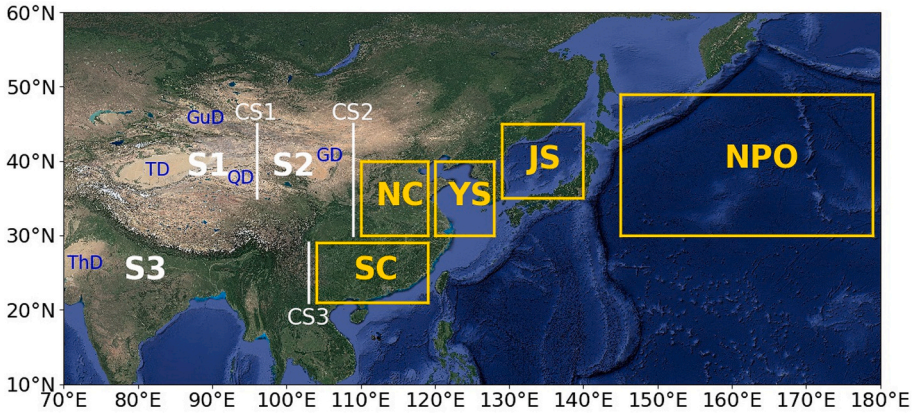

Fig. 1. The distribution of three dust sources over East and South Asia and five transport regions interested in this study. Three dust sources include that: S1: the Taklimakan Desert (TD), the Gurbantunggut Desert (GuD), and Qaidam Desert (QD); S2: the Gobi Desert (GD); S3: Thar Desert (ThD). Five transport regions are the North China (NC: [30-40°N, 110-119°E]), the South China (SC: [18-30°N, 103-119°E]), the Yellow Sea (YS: [30-40°N, 120-128°E]), the Japan Sea (JS: [35-45°N, 129-140°E]), and the northwest Pacific Ocean (NPO: [30-50°N, 145-180°E]), respectively. The downstream contribution of three dust sources will be evaluated at three meridional cross-sections (white lines) of 95 °E for S1 (CS1), 110 °E for S2 (CS2), and 103 °E for S3 (CS3), respectively.

latitudinal and longitudinal horizontal resolution of 1.9° and 2.5°, respectively, was used to convert the DMC profiles from the CALIOP-based dust extinction coefficient (DEC) at 532 nm (see Section 2.2). Fig. 2 shows the seasonal climatology of Asian dust MEE ($m^2\ g^{-1}$). The lower dust MEE related to the dust source and adjacent transport region and increased with the transport distance. This agrees well with other research (Hand and Malm, 2007; Kaufman et al., 2005) and results from there being a significant inverse correlation between the dust MEE and particle size (Ansmann et al., 2011; Wang et al., 2021a).

2.2. MERRA-2 dataset

The MERRA-2 dataset was produced by coupling the Goddard Earth Observing System version 5 (GEOS-5) with the Goddard Chemistry Aerosol Radiation and Transport (GOCART) model (Gelaro et al., 2017). It assimilates not only meteorological observations but also the aerosol optical depth at 550 nm, which is derived from various ground- and space- borne remote sensing platforms, such as the Aerosol Robotic Network (AERONET), the MODIS, the Advanced Very High Resolution Radiometer (AVHRR), and the Multiangle Imaging Spectroradiometer (MISR) (Randles et al., 2017). The MERRA-2 wind field data can also effectively reproduce the main characteristics of the tropospheric horizontal wind, especially in winter and summer. This is highly correlated with observations by stratosphere-troposphere wind profiler radar (STR) at 205 MHz, with a correlation coefficient of up to 0.9 (Sivan et al., 2021). In this study, the daily aerosol and meteorological products from

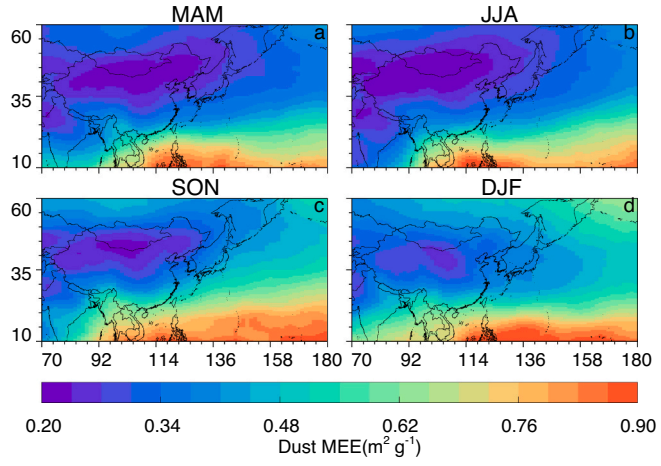

Fig. 2. The climatology of dust MEE over Asia from DustCOMM dataset in (a) spring (March-April-May, MAM), (b) summer (June-July-August, JJA), (c) autumn (September-October-November, SON), and winter (December-January-February, DJF).

the MERRA2 reanalysis, which have gridded resolutions of 0.5° at latitude and 0.625 ° at longitude, were used to provide information relating to the horizontal wind field and DMC at several pressure levels to calculate the dust transport flux. The column-integrated DOD and DMC were also used to explore the Asian dust distribution and to compare it to that derived from CALIOP.

2.3. Total dust extinction profiles derived from CALIOP

The CALIOP, onboard Cloud-Aerosol Lidar and Infrared Pathfinder Satellite Operations (CALIPSO) satellite, provided accurate aerosol types and vertical structure at a global scale by using the advantages of polarization lidar (Winker et al., 2009). The quality of Version 4 product was significantly improved, especially for the daytime. In this version, the daytime calibration biases were reduced by lifting the molecular normalization region from 30–34 km in Version 3 to 36–39 km (Gross et al., 2016; Omar et al., 2009b). To better characterize the total dust aerosol, we thus employed the all-day aerosol profiles in Version 4.2, level 2 covering a 12-year period from 2007 to 2018, at a nominal resolution of 5 km along the track and vertical resolution of 60 m in the troposphere. A cloud-aerosol discrimination score of between −70 and −100 (Liu et al., 2019) and extinction quality control flag values of 0, 1, 2, 18, and 16 were first selected (Winker et al., 2013) to ensure high-quality retrieval. The backscatter coefficient profiles of dust, polluted dust and dusty marine were then separated from the total one according to the types of aerosols in the Vertical Feature Mask (VFM) products. As with Wang et al. (2020a) and Hayasaka et al. (2007), to exclude the contamination of non-dust aerosols in polluted dust and dusty marine, the total DEC (α_d) was then obtained from an assumed dust lidar ratio (S_d) and the total dust backscatter coefficient (β_d), which is separated from the total aerosol backscatter coefficient (β_a) according to the determined PDR for dust (δ_d) and non-dust (δ_{nd}) aerosol:

$$\alpha_d = S_d\beta_d = S_d\beta_a \times \frac{(\delta - \delta_{nd})(1+\delta_d)}{(1+\delta)(\delta_d - \delta_{nd})} \quad (1)$$

where, δ is the PDR observed by CALIOP. As in previous studies (Freudenthaler et al., 2017; Mamouri and Ansmann, 2014; Sugimoto et al., 2002), the values of δ_d and δ_{nd} in this study were set at 0.31 and 0.05, respectively, to avoid unnecessary exclusion or inclusion of dust events. The value of β_d was set at β_a or 0 for dust bins or non-dust bins, respectively. The S_d at 532 nm was set to 44 sr^{-1}, as in previous studies (Kim et al., 2018). The total DEC profile was then gridded with a resolution of 0.5° at latitude and 1.5° at longitude by a single aerosol species re-grid average approach that assumes extinction to be 0.0 km^{-1} for all other species prior to calculating the average dust extinction within a grid (Amiridis et al., 2013). This ensures a higher resolution, especially for the complex terrain around the Tibet Plateau, when seeking to understand the Asian dust distribution and transport pattern. It also

maximizes the number of samples, thereby guaranteeing that there are at least 150 dust-detection layer samples for each grid cell (over 800 for an individual grid) for the desert sources across all seasons and 50 for the long-range transport region in MAM and DJF (Fig. S1). The total DOD can then be calculated by integrating the DEC profile.

2.4. Dust transport flux and TCA estimates

The dust transport flux was estimated in a similar way to Yu et al. (2015a). First, we derived the DMC profiles ($m_d(z)$, g m^{-3}) from the total DEC ($\alpha_d(z)$) by using the seasonal dust MEE climatology (k_d) from the DustCOMM dataset as follows:

$$m_d(z) = \frac{\alpha_d(z)}{k_d} \tag{2}$$

Generally, the seasonally-varying dust MEE climatology can significantly improve the accuracy of the DMC estimation, when compared to an assumed fixed or linearly-varying MEE (Kaufman et al., 2005; Yu et al., 2015a). This is especially the case for long-range transported dust. In view of the accuracy of dust MEE in DustCOMM, the column-integrated values (weighted by the dust vertical distribution) were used in this study. The DML was defined as the integrated DMC profiles from the surface to 12 km. The dust flux rate (DFR, g m^{-1} s^{-1}) at each grid in the meridional (south-north, R_V) and zonal (west-east, R_U) directions was calculated separately:

$$R_V = \int_{z_1}^{z_2} m_d(z)V(z)dz \tag{3}$$

$$R_U = \int_{z_1}^{z_2} m_d(z)U(z)dz \tag{4}$$

where, $m_d(z)$ is the DMC at altitude z; z_1 and z_2 are the altitude ranges of interest for the DFR; $V(z)$ and $U(z)$ are the monthly-averaged meridional and zonal wind speed (m s^{-1}) at altitude z, which was taken from the MERRA-2 reanalysis dataset. A positive R_V and R_U represent a northward and eastward transport, respectively, and vice versa. To make it easier to understand, the overall DFR unit was unified to kg m^{-1} day^{-1} in the whole context, which are integrated to a daily scale. The monthly and seasonal dust transport flux at given altitude ranges of interest were then retrieved by multiplying the corresponding DFR and duration (day) in that month or season.

To ensure a better understanding of the seasonal evolution of the dust transport process over Asia, the mass-weighted dust TCA was extracted in a similar way to Meng et al. (2017). First, the boundary of the main dust transport belt was acquired using a Canny Edge Detector based on the seasonal DML spatial distribution. The DML threshold value of DMC was set at 0.05 g m^{-2}. For each grid with longitude k, we can get a dynamic southernmost and northernmost latitude of the dust transport belt. The central latitude (lat_k) was then calculated using the meridional DML weighted average (Meng et al., 2017):

$$lat_k = \frac{\sum_{i=1}^{n} m_{d,i} \times lat_i}{\sum_{i=1}^{n} m_{d,i}} \tag{5}$$

where, $m_{d,i}$ and lat_i are the DML and latitude of the corresponding grid, i, respectively; n is the number of grids within the boundary of the main dust transport belt at longitude k. As the main dust transport belt located in East Asia contributes more than 80% of the dust in Asia (Zhang et al., 2003b), the grids on the south side of the TP were ignored in the above calculation of the Asian dust TCA. Two heights, for 50% and 90% DMC, were calculated to respectively depict the vertical mass-weighted center and canopy of the dust layers along the dust TCA (as per Winker et al. (2013)).

2.5. Estimation of the downstream contribution of the desert sources

To estimate the downstream contribution of the East (S1 and S2) and South (S3) Asian desert sources, the integrated dust transport flux along three meridional cross-sections at 95 °E (CS1), 110 °E (CS2) and 103 °E (CS3) (shown in Fig. 1) were investigated in this study. Note that the composite DFR was used during the integration process, so as to fully capture the total dust transport in the zonal and meridional direction. However, it is worth noting that the above transport contribution of S2 will be overestimated because the dust aerosols from S1 are usually mixed with those of S2. The estimation for S2 therefore needs to be corrected to exclude the contribution of the dust aerosols from S1 in the cross-section for S2. As S2 is located in an arid and semi-arid region with an annual precipitation of less than 250 mm (Huang et al., 2015), we only consider the dry deposition process and ignore the wet removal process, so as to facilitate assessment of its contribution.

A schematic diagram of the correction process is shown in Fig. 3. First, we calculate the dust lost fraction (f_D) caused by the dry deposition process at CS1, that is, a ratio of dust dry deposition flux (F_D) to the integrated transport flux for CS1 (F_1):

$$f_D = \frac{F_D}{F_1} = \frac{1}{F_1}\sum_i m_{d,i}(z_0)V_D S_i \tag{6}$$

where, $m_{d,\,i}(z_0)$ and S_i represent the near-surface DMC and area of the corresponding grid, i, along the CS1, respectively. Here, we assume that the dust is well-mixed from the surface to 300 m and, in addition, $m_{d,\,i}(z_0)$ is taken to be the average of DMC in this range, thereby minimizing the CALIOP retrieval errors near the surface. V_D is the dry deposition velocity, assumed to be 0.02 m s^{-1}, which is consistent with the figures proposed by Wang et al. (2012) and the observations of Hsu et al. (2009) for Asian dust in the East China Sea. We also assume that the f_D remains constant along the dust TCA from 95 °E to 110 °E. So, the dust transport flux of S1 at each grid ($F_1{}^k$) along the dust TCA and the net dust transport flux (F_2*) of S2, excluding the contribution of S1, can be calculated respectively as follows:

$$F_1^k = F_1 \times (1 - f_D)^k (k = 0, \ldots, \mathrm{n}) \tag{7}$$

$$F_2^* = F_2 - F_1^n \tag{8}$$

where, F_2 and $F_1{}^n$ represent the integrated total dust flux at CS2 and the integrated transport flux of S1 at cross-section CS2, respectively; and n is the number of grids between CS1 and CS2 along the dust TCA. The seasonal and annual downstream contribution of each desert source can also be estimated by multiplying the corresponding duration.

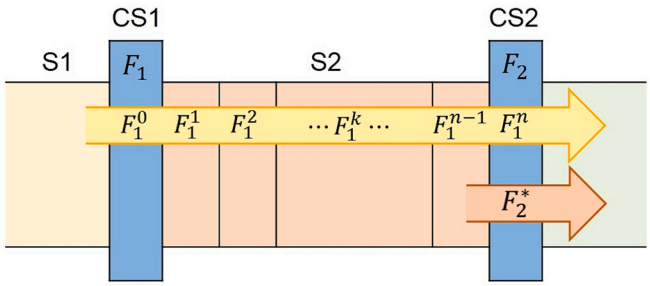

Fig. 3. Schematic diagram of the dust transport flux correction of S2. The yellow and red arrows indicate the transport contribution of S1 and S2 to the downstream, respectively. F_1 and F_2 are the integrated dust transport fluxes for the cross-sections CS1 and CS2. $F_1{}^k$ represents the transport flux of S1 at grid k along the dust TCA. F_2* is the corrected downstream contribution of S2.

3. Results

3.1. Asian DML and TCA climatology

The CALIOP and MODIS observations, MERRA-2 reanalysis, and DustCOMM datasets were used together to characterize the horizontal distribution of Asian dust. Fig. 4 shows the resulting climatology for the seasonal-mean DML across the area principally affected by Asian dust (from 70°E to 180°E). The horizontal evolution of the DML, with significant seasonal variation, can be seen clearly, moving from the source regions downwind to northern and eastern China and even the NPO. This is highly consistent with the measurements and modeling of the DOD (Fig. S2). Similar results have been documented in previous studies (Alizadeh-Choobari et al., 2014; Guo et al., 2017; Huang et al., 2007; Zhang et al., 2003a). The DML peaks mainly occurred at the natural dust sources, e.g., the TD, GD, and Thar Desert, and the anthropogenic dust sources, e.g., the North China Plain where there is a large amount of human activity (Huang et al., 2015), with these contributions being pure and polluted dust, respectively (see Fig. S3). The annual-mean DML for these four typical regions was about 0.51, 0.21, 0.68, and 0.28 g m^{-2}, respectively. Dust aerosols over the TD and GD were also transported into the Pacific Ocean, under the influence of the western Pacific subtropical high and the Aleutian Low (Uno et al., 2011), with a maximum DML of 1.18 g m^{-2} in MAM, followed by JJA (0.73 g m^{-2}) and DJF (0.42 g m^{-2}). Similarly, a dust belt dominated by polluted dust (Fig. S3), especially in MAM, extended from the Indo-Gangetic Plain, across the Yunnan-Guizhou Plateau and to eastern China. This may imply the transport of South Asian dust to eastern China and even the Pacific Ocean, in addition to the Tibetan Plateau (Wang et al., 2021b).

Although the seasonal migration of Asian dust can be demonstrated overall by the DML and DOD derived from CALIOP, the MERRA-2 reanalysis and DustCOMM dataset, there are significant differences between them. Compared to the CALIOP observations, the DML and DOD of MERRA-2 are larger than that of CALIOP over the East Asian dust source and its adjacent areas, especially in MAM and JJA. MERRA-2 may be limited by its dependence on the dust size and how the emission scheme was setup for the model used to produce the MERRA-2 dataset, as suggested by Gueymard and Yang (2020) who undertook observations and simulations. Conversely, the DML and DOD over the anthropogenic dust source (e.g., the North China Plain) and the long-range transport region (e.g., the NPO) by MERRA-2 across all seasons were significantly smaller than that of CALIIOP (see the middle column of Fig. 4 and the third column of Fig. S2). This can be mainly attributed to overestimation of dry and wet deposition (Wu et al., 2020). Also, the DustCOMM dataset shows consistent distribution characteristics with that of MERRA-2 (see the right column of Fig. 4 and Fig. S2).

To better understand variations in the Asian dust transport routes, the vertical-column integrated and mass-weighted dust TCA at different seasons were defined. These are superimposed on Fig. 4 using white lines. These dust TCAs run all the way through the natural and anthropogenic dust sources in northern China throughout the year, appearing as a curve for the TD, Hexi Corridor, GD, Northern China, and NPO. This reveals that the TD and GD are the greatest contributors for the total DML column. Large amounts of dust aerosols emitted from the TD and GD are transported to downstream areas along the dust TCA, mixing with anthropogenic dust over North China to form a heavy dust loading

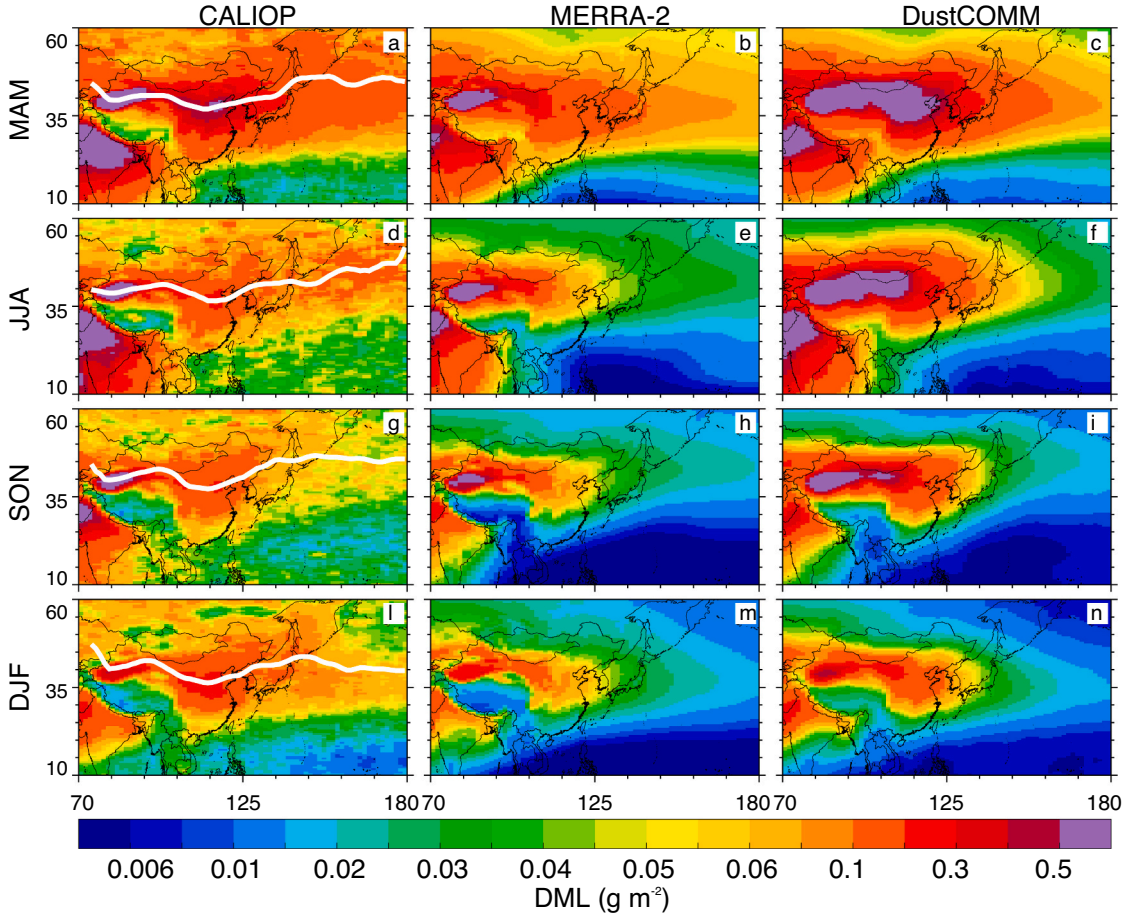

Fig. 4. The seasonal climatology of DML from CALIOP (left) and MERRA-2 (middle) and DustCOMM dataset (right) in (a-c) MAM, (d-f) JJA, (g-i) SON, and (l-n) DJF. The white lines represent the column-integrated dust TCA.

belt across mainland China and the Pacific Ocean. However, there is a significant northward or southward shift for the dust TCA over the long-range transport regions as the season changes, especially in the Pacific Ocean. The dust TCA arrives at its northernmost latitude of 50°N in JJA, while its southernmost latitude of 35°E is in DJF. These shifts are probably associated with the evolution of the subtropical high and Aleutian low over the western Pacific (Uno et al., 2011).

In view of how the complex terrain over Asia can affect the dust transport process, the vertical DML variation and dust TCA for different seasons were also assessed. Fig. 5 shows the seasonal DML and dust TCA climatology at 0-2.5, 2.5-5.0, 5.0-7.5, and 7.5-10 km, respectively. In general, the heavier DML concentrates at a lower altitudes and decreases as the altitude increases, regardless of the dust source or transport region. The DML over TD is significantly greater than it is over GD. The zonal dust transport belt, stretching from northwest China to the Pacific Ocean, can be clearly seen in both the surface and upper layers throughout the year, especially in MAM and DJF. The mass-weighted dust TCAs in the lower layer (< 5 km) are similar to those visible in Fig. 4. This further confirms that more DML concentrates in the lower layers. As the altitude increases, the TCAs gradually follow a zonal straight line due to the strong westerly winds above 5 km, with their location undergoing a southern shift over the TD and a northward or southward shift over the NPO.

3.2. Dust transport flux climatology

To properly estimate the dust transport flux, both the zonal and meridional DFR in the atmospheric column were calculated. Fig. 6 shows a composite of the column-integrated zonal and meridional DFR derived from CALIOP 2007-2018. The mass-weighted dust TCA is superimposed on top. The magnitude (color scale) and direction (vector arrow) of the dust transport and its seasonal changes are clearly visible. The typical DFR (>100 kg m^{-1} day^{-1}) is mostly distributed in the range of 30-50°N, with its maxima mainly appearing in MAM and DJF. The distribution of the dust TCA totally corresponds to the area with a higher DFR. However, the dust TCA over the dust source is located at the southern edge of the higher DRF. This can be attributed to the accumulation of a large amount of dust carried by the northwest winds at the northern foot of the Qinghai-Tibet Plateau. Contrariwise, the dust TCA over the Pacific Ocean is located at the northern edge of the higher DRF. This is caused by the combined action of the subtropical high and the Aleutian low, resulting in a southwest wind transport (Uno et al., 2011). The DFR over GD is noticeably larger than it is over TD, with a maximum of 250 kg m^{-1} day^{-1} in the northwest direction throughout MAM. This phenomenon similarly exists in the DFR profiles of S1 and S2 (as shown in Fig. S4). There are larger positive DFRs over GD than that over TD in the atmospheric column throughout the year. This means that the northwest wind can carry large amounts of dust across the China-Mongolia border and affect most areas of China, especially northern China. However, it is worth noting that the large negative DFR over TD appears below 3 km, especially in MAM (Fig. S4a) and JJA (Fig. S4b), which implies a potential dust backflow phenomenon in the Tarim Basin, due to the dynamic forcing of the east wind near the surface (Zhou et al., 2020a).

The transcontinental transport of dust from Central Asia and South Asia to the Tibetan Plateau, mainland China, and even the Pacific Ocean, should also not be ignored. As shown in Fig. 6a, a large number of dust aerosols emitted from Central Asian sources can be transported not only across the Pamir plateau and Tianshan Mountains, but also across Kazakhstan, Russia and Mongolia, with a subsequent impact on northwest and northern China, especially in MAM, where the DFR is 90 kg m^{-1} day^{-1} and SON, with a DFR of 70 kg m^{-1} day^{-1}. Under the prevailing northwest winds, these dust aerosols can affect the northeastern Tibetan Plateau, northern China, and the Pacific Ocean, together with local dust from East China. South Asian is not only lifted into the TP across the Himalayas under the co-configuration of upper- and lower-air circulation (Wang et al., 2021b), but also across the Hengduan Mountains and the Yunnan-Guizhou Plateau, meeting up with the East Asian dust in southern China and producing a higher DFR of 150 kg m^{-1} day^{-1} in MAM.

The vertical variation in the DFR clearly reflects differences in the dust transport downstream from various dust sources. Fig. 7 shows the seasonal climatology in terms of the magnitude and direction of the DFR at 0-2.5, 2.5-5.0, 5.0-7.5, and 7.5-10 km. Generally, as the altitude increases, the DFR decreases significantly across the seasons, whatever the source or transport area. An exception is TD, where it initially increases, then decreases. This is closely related to the terrain and atmospheric circulation. Note also that, unlike the DML distribution in Fig. 5, the DFR over GD is significantly greater than it is for TD in MAM and DJF. This

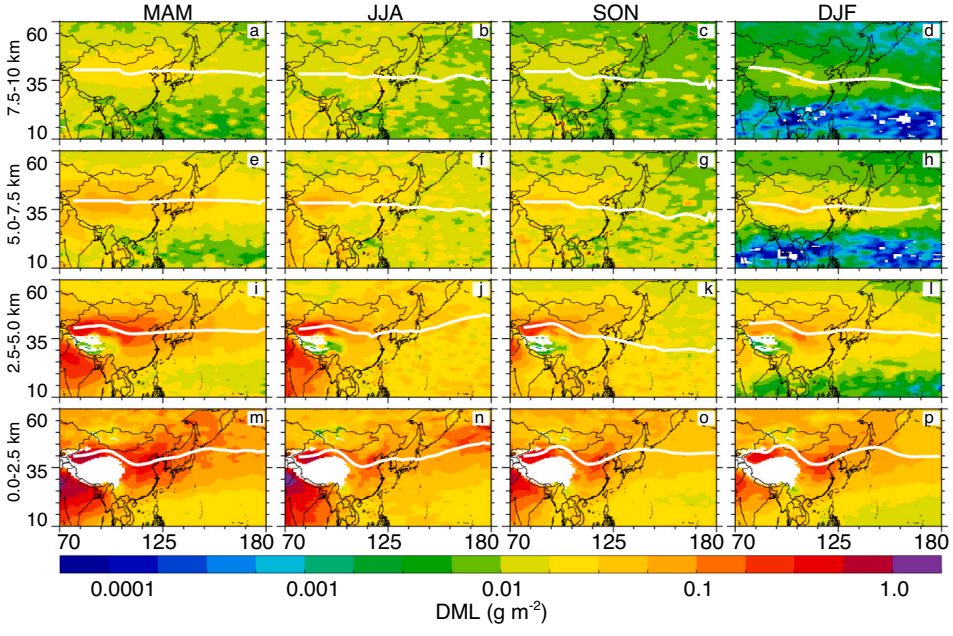

Fig. 5. Same as Fig. 4 but for the layer-integrated DML in the (a-d) 7.5-10 km, (e-h) 5.0-7.5 km, (i-l) 2.5-5.0 km, and (m-p) 0-2.5 km during different seasons. The white lines represent the layer-integrated dust TCA.

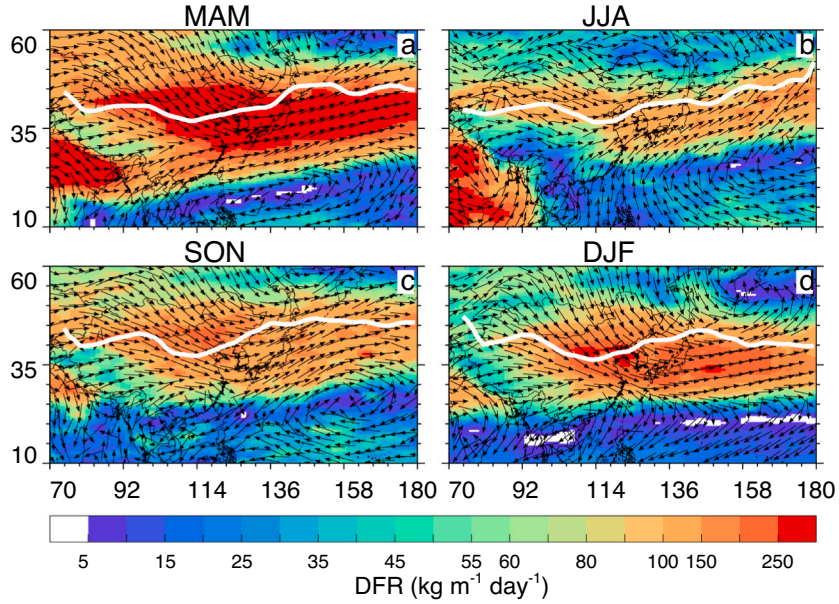

Fig. 6. A composite of column-integrated zonal and meridional DFRs (kg m^{-1} day^{-1}) derived from CALIOP 2007-2018 climatology, showing the magnitude (color scale) and direction (arrow of vector) of dust transport in the atmosphere and its seasonal variations. The white lines represent the mass-weighted dust TCA.

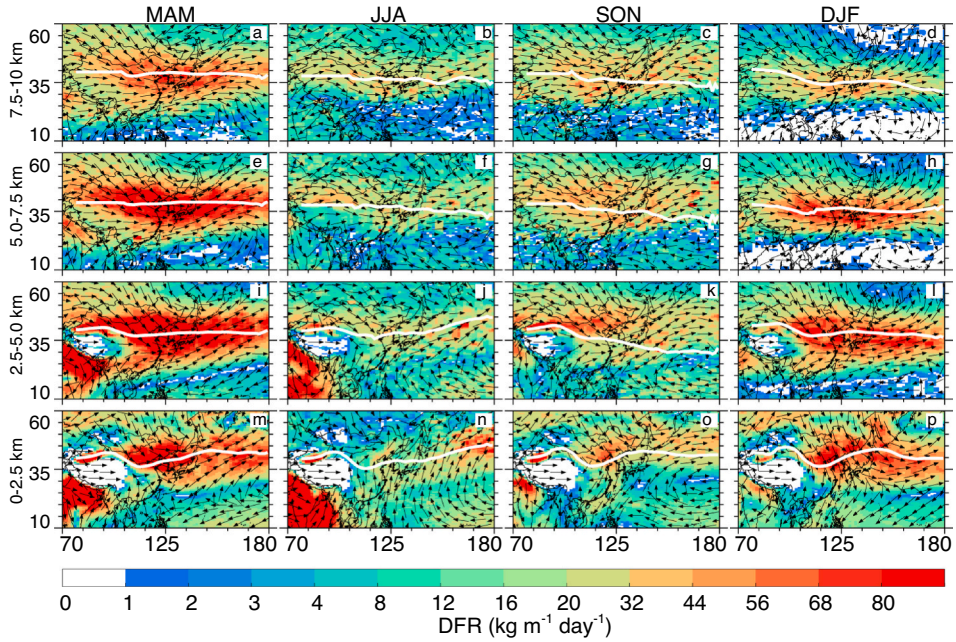

Fig. 7. Same as Fig. 6 but for the composite of layer-integrated DFR (kg m^{-1} day^{-1}) at (a-d) 7.5-10 km, (e-h) 5.0-7.5 km, (i-l) 2.5-5.0 km, and (m-p) 0-2.5 km during different seasons. The white lines represent the layer-integrated dust TCA.

suggests that the dust aerosols over GD are more easily transported downstream, while, over TD, they have to be lifted to a certain height and then carried away by the northwest winds. The dust transport direction shows significant seasonal and vertical differences and tends to match the zonal direction as the altitude increases. This is consistent with the layer-integrated TCA. A significant transcontinental transport of South Asian dust can also be clearly observed at 2.5-5 km, especially in MAM and DJF.

To better characterize the vertical evolution of the dust transport process over Asia, Fig. 8 depicts the vertical distribution of the DMC and DFR in the zonal and meridional directions along with the column-integrated dust TCA over all four seasons. The mass center (solid line) and canopy (dashed line) of the dust layer in a vertical direction are also indicated by the 50% and 90% DMC, respectively. Overall, 90% of the mass canopy of the dust layer is trapped below 6 km in MAM, 5 km in JJA and SON, and 4 km in DJF. With the increase of transport distances, the mass canopy (dashed lines) shows a wave-like decrease along the dust TCA as a result of changes in the terrain and the dry and wet removal process, especially in JJA and SON. The variation in the dust mass center is fully consistent with the canopy, but is trapped below 3 km. Although the largest DML associated with the dust TCA occurs in TD (73-92 °E) throughout the year, the dust transport flux is not at its maximum here, and there are significant changes in the transport direction, as shown in the middle panel of Fig. 8. The dust aerosols over TD

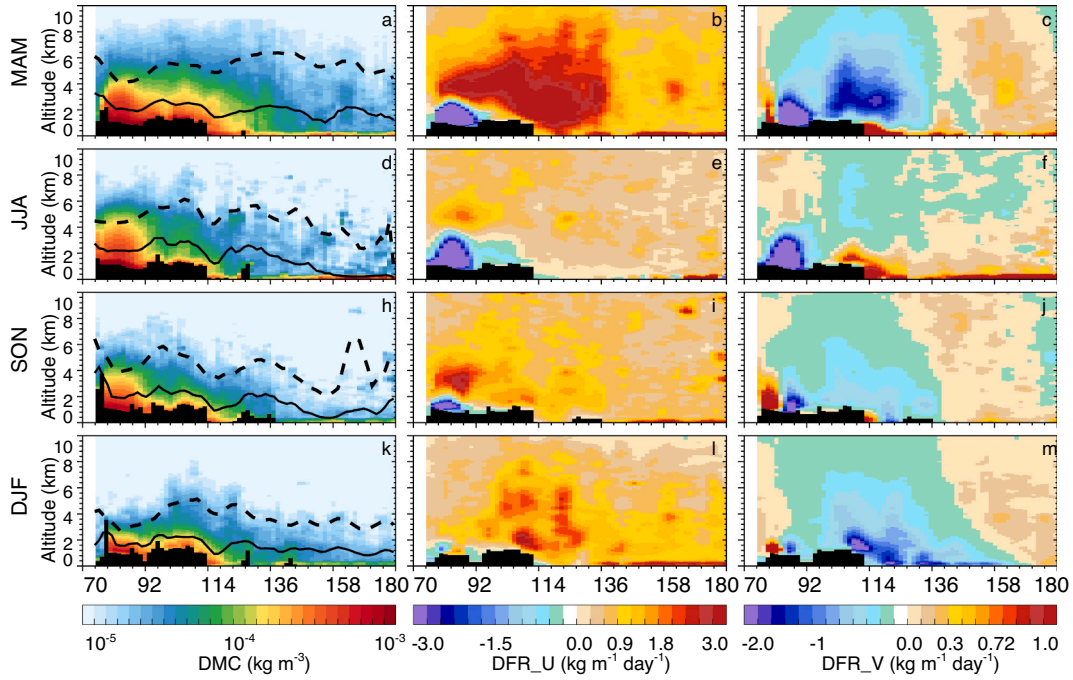

Fig. 8. Vertical distribution of the seasonal climatology of DMC (left), zonal (middle) and meridional (right) DFR derived from CALIOP along the column-integrated dust TCA. The positive DFR indicates eastward or northward transport, but the negative indicates the opposite. The black lines indicate that the 50% (solid line) and 90% (dashed line) DMC lies the height below, respectively.

are generally transported westward and southward (giving a negative DFR) under 2.5 km in MAM, 4 km in JJA, and 2 km in SON and DJF. This encourages an accumulation of dust on the north slope of the Tibetan Plateau. Dust aerosols can be transported eastward to affect downstream areas when they are lifted above these heights. However, dust aerosols at all altitudes over GD and North China (95-120 °E) are transported eastward and southward in their entirety, apart from a northward transport near the surface in JJA. When dust aerosols travel eastward over the Sea of Japan (135 °E), the DFR changes from negative to positive in the meridional direction, that is, they travel northeast to the North Pacific under the effect of atmospheric circulation.

3.3. Contribution of Asian desert sources

As discussed in Sections 3.1 and 3.2, there are significant differences in the DML and DFR over the East and South Asian desert sources and downstream transport regions, regardless of seasonal or vertical distribution. However, the contribution of different desert sources to the mainland of China and adjacent seas remains an open question. As described in Section 2.5, we used the integrated dust transport flux along three meridional cross-sections to address this question. Fig. 9 shows the climatology of the net dust transport flux (as a table) and the relative downstream contribution (as pie charts) for S1, S2 and S3 at seasonal and annual scales. It will be recalled that the downstream contribution of S2 was corrected by assuming dry deposition and ignoring the wet removal of dust particles, implying that the dust transport flux from S1 to S2 is overestimated, while that of S2 is underestimated. Nonetheless, the downstream contribution of S2 is still the largest of the three desert sources. The annual dust transport flux of S2 is 145.88 Tg, about 2.1 and 4.8 times that of S1 (68.40 Tg) and S3 (30.43 Tg), respectively. There are significant seasonal differences, with the largest figure being in MAM (64.76 Tg), followed by DJF (36.41 Tg), and then SON and JJA. Note that S1 and S3 have similar season variations, though the dust transport flux for S1 in SON is larger than DJF. This may be related to the long-range transport at higher altitudes. Although S2 has the smallest annual-mean dust mass load of 0.21 g m^{-2} out of all the Asian deserts, it

	MAM	JJA	SON	DJF	Annual
S1	27.90 (7.90)	12.58 (4.01)	15.54 (4.36)	12.38 (3.63)	68.40 (19.90)
S2	64.76 (11.52)	17.00 (3.95)	27.21 (4.95)	36.41 (5.75)	145.88 (26.17)
S3	16.29 (3.21)	2.18 (0.43)	5.18 (1.05)	6.78 (1.49)	30.43 (6.18)

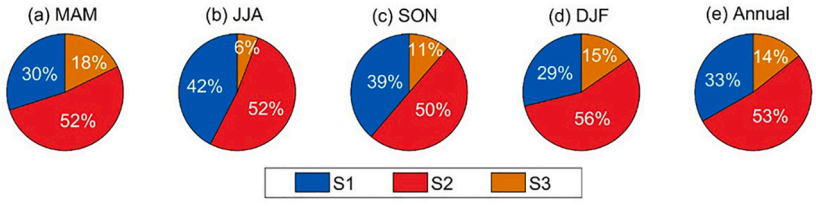

Fig. 9. The net dust transport flux (shown in table, unit: Tg) and relative contribution (pie charts) of East (S1 and S2) and South (S3) Asian desert sources to the mainland of China and adjacent sea area. The numbers in parentheses represent the uncertainty caused by one standard deviation of dust MEE.

produces the greatest downstream dust transport flux, followed by S1 and S3, accounting for about 68% in East Asia and 60% in Asia overall. If we represent the contribution of the different desert sources in Asia to mainland China and its adjacent seas by using the transport flux in the three cross-sections, the East Asian deserts (S1 and S2) contribute up to 88% overall, which is significantly greater than that of the South Asian deserts (S3). The CALIOP-based quantification of the East Asian dust contribution is generally consistent with the results of model simulations, though there is a slight bias. For example, Zhang et al. (2003b) estimated that the deserts in Mongolia and western and northern China contribute about 80% of the total Asian dust emissions, based on size-dependent soil dust emission and transport model simulations. There are two possible reasons for the bias, (1) the net dust aerosol transport flux for S1 and S2 was overestimated as a result of ignoring the wet deposition process, or (2) the transcontinental dust aerosol transports from Central Asia at the western side of S1 and northern side of S2 (as shown in Fig. 6a) need to be excluded.

To better assess the downstream contribution of the East and South Asian deserts, the DMC and composite DFR vertical distributions along the meridional cross-sections were analyzed, as shown in Figs. 10-12. For S1 (Fig. 10), the overall zonal DFRs reveal a significant eastward transport through the Hexi Corridor and the Qaidam Basin throughout the year, apart from a slight westward transport near the surface. The most significant downstream contribution of S1 occurs at an altitude of 2-6 km from 36-42 °N, but is at 4-6 km over the Tibetan Plateau (35 °N), which differs from the decrease in the DMC with height. The altitude of the maximum DFR varies according to the season, especially over the Hexi Corridor, with it concentrating at 2-4 km in DJF (Fig. 10m) and 4-6 km in JJA (Fig. 10e). The integrated DRF along CS1 initially increases, then decreases with height, with the maximum DFR of 49 kg m^{-1} day^{-1} being at 4.5 km in MAM (Fig. 10c) and 28 kg m^{-1} day^{-1} at 6 km in DJF.

However, in the case of S2 (Fig. 11), in addition to it having a larger net zonal dust transport flux than S1 (Fig. 10), the vertical distribution of the downstream contribution is significantly different. Higher DFR levels (> 0.9 kg m^{-1} day^{-1}) occur throughout the range from the surface to 9 km and extend southward from 44°N to 29°N, especially in MAM and DJF. This is a significantly wider distribution than that of S1. The integrated DFR along CS2 decreases overall with an increase in altitude, except in JJA, as shown in the middle and right panels in Fig 11. The maximum DFR appears at 2.5 km in MAM, 2.0 km in SON, and 2.0 and 4.5 km in DJF. This is lower than the figures for S1, suggesting that dust aerosols from S1 and S2 can be transported downstream at different altitudes, affecting wider areas, such as the Pacific Ocean and even North America (Naeger et al., 2016).

For S3, the overall zonal DFRs in CS3 show a significant eastward transport across the Hengduan Mountains and the Yunnan-Guizhou Plateau, especially in MAM and DJF (Fig. 12). The most significant dust transport from S3 to China occurs at an altitude of 3.5 km, from 21-28 °N in MAM. This moves southward to18-23 °N in DJF and is accompanied by a decrease in the DFR. This suggests that, in addition to dust aerosols, other pollutants (e.g., coal combustion, biomass burning) over South Asia can be effectively transported by the prevailing westerlies into southern China and affect the haze pollution levels. This finding is fully consistent with chemical composition analyses and the source apportionment of $PM_{2.5}$ in Kunming City in China (Zhou et al., 2020b). Zhou et al. (2020b) found that the concentrations and fractions of Ca^{2+} and Mg^{2+} in spring were much higher than in other seasons, with them being mainly derived from soil dust (Shen et al., 2010), having been released into the atmosphere during biomass burning and dust emission.

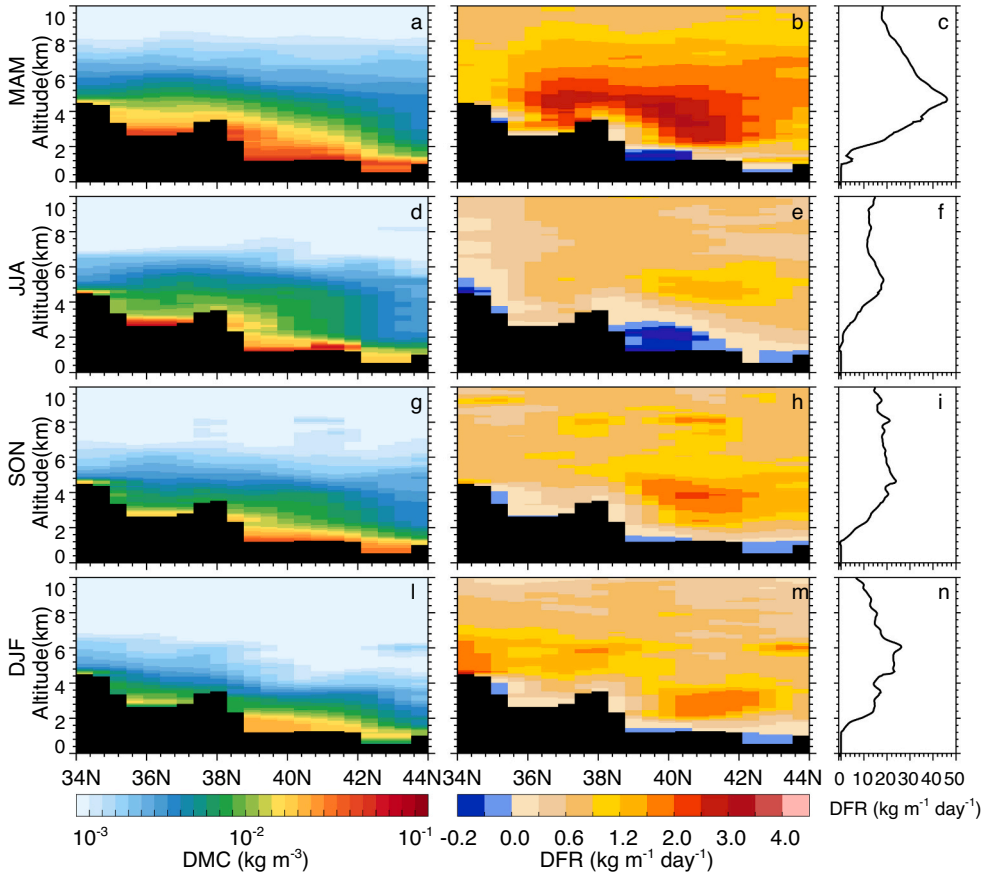

Fig. 10. Vertical distribution of seasonal climatology of DMC (left) and composite of DFR (middle) derived from CALIOP along the meridional cross-section of 95 °E (CS1). The profiles of integrated zonal DFR along the border at different seasons are also shown (right).

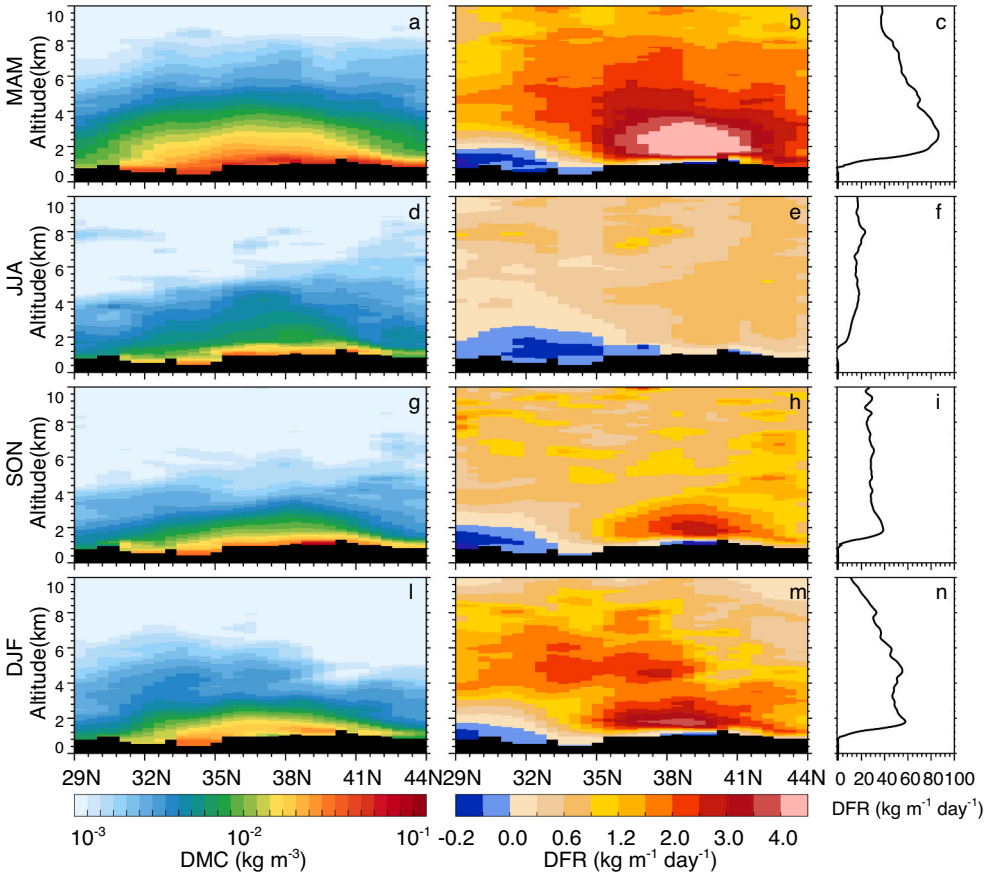

Fig. 11. Same as Fig. 9 but for the meridional cross-section of 110°E (CS2).

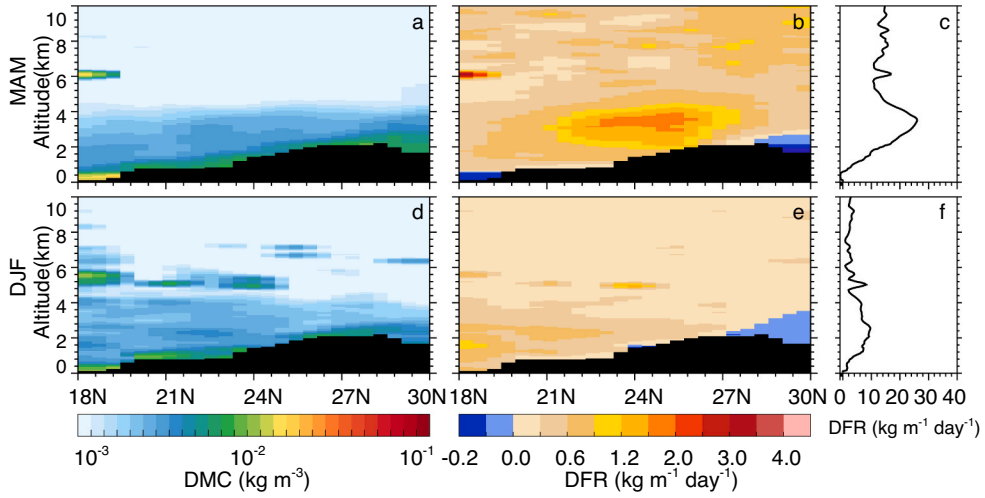

Fig. 12. Same as Fig. 9 but only for the meridional cross-section of 103 °E (CS3) at MAM and DJF.

In addition, a DFR stratification phenomenon can be observed, especially at higher altitudes, for both S1 and S2 throughout the year (see Figs. 10 and 11). This is because the higher DFR not only depends on the DMC but also the wind speed, although the DMC decreases with an increase in altitude. During DJF, two distinct transport layers with different depths and DFR levels can be observed below and above 4 km in CS1 and CS2. This clearly indicates a superposition of local and long-range transported dust on the downstream flow (Sugimoto et al., 2019). In addition, although the integrated DFR above 6 km along CS1 and CS2 in JJA and SON is generally small (~0.3-2.5 kg m^{-1} day^{-1}), the downstream contribution of dust cannot be ignored, with it accounting for 42% and 41% of the column transport flux for S1 in JJA and SON, and 29% and 31% for S2, respectively.

3.4. Dust budget of typical transport regions

As discussed in Section 3.3, dust aerosols from East and South Asia can be transported to northern and eastern China and the adjacent seas

by the prevailing westerlies. While an accurate assessment of dust deposition over oceanic areas can assist with estimation of the deposition flux of nutrients (e.g., ferrum, phosphorus, nitrogen, and so on) carried by dust aerosols, thereby enhancing evaluation of the role of dust in the oceanic biogeochemical cycle (Maki et al., 2021; Schepanski, 2018; Shi et al., 2012; Zhang et al., 2020). In general, the deposition fluxes of these nutrients are estimated according to their constituent proportions in dust deposition fluxes (e.g., Jickells et al., 2005; Schulz et al., 2012). In this study, the dust budget over five typical transport regions along the dust TCA was estimated, as in Yu et al. (2015b), by using the net inflow/outflow in latitudinal and longitudinal cross-sections, which can reflect the net difference between the deposition and emission of dust aerosols at the defined areas. For oceanic areas, where there is no dust emission, the total dust deposition into the ocean can be best represented by the dust budget. Taking into account the difference in the area of the transport regions, the dust budget rate was defined as the ratio of the total dust budget to the size of the region. This can be used to evaluate the contribution of dust deposition in these regions.

Fig. 13 shows the annual and seasonal dust budget climatology (bar plot) and budget rate (red line) for the five typical transport regions in the Asian dust TCA. North China (NC) and South China (SC) are terrestrial regions typically affected by Asian dust. The superposition of the natural dust transport and local anthropogenic dust emission reveals a more pronounced DOD center in NC (Fig. S2). We set the southern boundary of NC at 30 °N to distinguish SC, as they can be jointly affected by East and South Asian dust (Fig. 6a). The annual dust budget for NC (18.01 Tg), with a maximum of 7.74 Tg in MAM and 5.48 Tg in DJF, is significantly greater than it is for SC (3.06 Tg), with a maximum of 1.75 Tg in MAM. The annual dust budget rate for NC is about 21.58 g m^{-2}, which is again significantly larger than it is for SC (2.75 g m^{-2}). This means that the climatic and environmental impact of Asian dust is much greater in NC than in SC. The annual dust budget of the three adjacent seas, the Yellow Sea (YS), the Japan Sea (JS), and the NPO, was 29.76, 20.82, and 26.01 Tg, respectively. Disregarding local dust emissions, the dust budget in these oceanic regions may well represent the total dust deposition into the ocean. The annual dust deposition in NPO is slightly higher than it is in YS and JS. This is mainly because it covers a larger area. The corresponding annual dust budget rates were 40.12, 20.41, and 4.01 g m^{-2}, respectively. Generally, both the seasonal and annual dust deposition rate decreases as the transport distance increases, as a result of dry and wet deposition processes.

4. Uncertainties relating to the CALIOP-based DMC retrieval

Although high-quality datasets were employed in this study, i.e., the CALIOP V4 measurements, the MERRA-2 wind data, and the DustCOMM MEE, there are inevitable uncertainties in estimating the DMC and dust transport flux for the Asian dust sources and their transport regions. These relate in particular to the separation of dust from non-dust aerosols, the estimation of dust extinction, and the setting aside of vertical changes in the dust MEE. We discuss each of these below, to help readers to acquire a more objective understanding of our findings and conclusions.

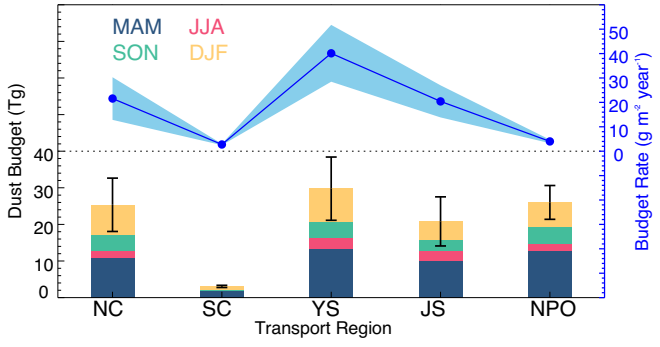

Fig. 13. The climatology of annual and seasonal dust budget (bar plots, unit: Tg) and budget rate (blue line, unit: g m^{-2} $year^{-1}$) over five typical transport regions along Asian dust TCA. The error bars represent the uncertainty of annual dust budget caused by MEE with one standard deviation.

4.1. Uncertainties regarding dust separation

To fully characterize the dust aerosols floating in the atmosphere, all the dust-type aerosols (e.g., dust, polluted dust, and dusty marine) classified by CALIOP along the Asian dust TCA were included in this study. We separated dust from non-dust aerosols by using the CALIOP PDR measurements. This was based on a priori knowledge of the expected PDR for dust and non-dust aerosols. We had to do this because there is a significant mix of dust and anthropogenic pollutants in Asian dust. However, the PDR values associated with dust and non-dust aerosols vary according to the physical and chemical properties of the aerosol particles (Sugimoto and Huang, 2014; Wandinger et al., 2010). Surface-based lidar observations show that East Asian dust has a higher PDR (0.31) than non-dust (Freudenthaler et al., 2017; Sugimoto et al., 2002). The PDR can also decrease as the particle sizes decrease during long-range transport. Non-dust has a non-negligible PDR of up to 0.07, depending on the type of non-dust aerosol and its hygroscopicity (Yu et al., 2015a). Thus, the a priori assumption of the PDR for dust (0.31) and non-dust (0.05) in this study constitutes an important source of uncertainty when separating dust from non-dust aerosols using the PDR measurement. Yu et al. (2015a) estimated the relative uncertainties regarding the trans-Atlantic dust transport flux associated with their dust and non-dust separation scheme, which was based on two sets of PDR thresholds for dust and non-dust to represent the lower- and upper-bound estimation of dust extinction and mass flux. This was over ±15% and even increased with transport distance.

4.2. Uncertainties regarding dust extinction

The accuracy of the CALIOP-based dust extinction profile is not only related to its capacity to detect dust aerosols, but also depends on the assumed dust lidar ratio. Most studies show that the official cloud-aerosol discrimination algorithm can correctly identify dust aerosol (Omar et al., 2009a; Tesche et al., 2013), but sometimes heavy dust storms are misclassified as clouds (Luo et al., 2015; Pan et al., 2020). So, when the dust layer is below thick opaque cloud or its DOD is over 3, it is hard to obtain an accurate and complete dust profile because the CALIOP lidar signal can be completely attenuated (Hu et al., 2007). Apart from this, some tenuous aerosol layers are difficult to detect for CALIOP, especially in the North Pacific (Song et al., 2021). This can result in underestimation of dust samples and dust transport flux over desert sources, where there are frequent heavy dust storms (An et al., 2018; Fu et al., 2008), and over the Pacific Ocean, where there is a high occurrence of cloud (Uno et al., 2011) or tenuous aerosol layers. These uncertainties cannot be assessed because there are no available observations. In addition, it should be that CALIOP V3's operational AOD shows an underestimation of about 30% when compared to AERONET clear-sky measurements (Omar et al., 2013). The updated V4 AOD increased by 0.044 (0.036) or 52% (40%) for nighttime (daytime) because of the increase in the lidar ratio (Kim et al., 2018), so the AOD discrepancies between CALIOP and AERONET or MODIS were reduced in V4, when compared to V3. In this study, the new averaged lidar ratio of 44 in the CALIOP V4 dataset (Kim et al., 2018) was assumed, which is consistent with observations from ground-based Raman lidar observations over TD (Hu et al., 2020) and Central Asia (Hofer et al., 2020). Therefore, any uncertainties regarding dust extinction are mainly caused by deviation (±9) in the lidar ratio, which is about ±20% (Wang et al., 2021a).

In view of the above uncertainties, such as how best to separate dust from non-dust based aerosols and the most effective lidar ratio assumption, accurate partition of the CALIOP-based DOD from AOD is an important prerequisite for quantitative research on the Asian dust cycle. The CALIOP DOD was compared to that of MERRA2 reanalysis and DustCOMM dataset in Section 3.1. A MODIS-based DOD partition from AOD was also employed to indirectly verify the accuracy of the CALIOP DOD Partition from AOD. The MODIS DOD over the ocean was estimated by using the AOD and fine mode fraction, as retrieved by the Dark Target algorithm, while the MODIS DOD over the land was estimated by using the AOD, Ångström exponent, and single-scattering albedo at 470 nm, as retrieved by the Deep Blue algorithm. The detailed method matched that used by Song et al. (2021). It is worth noting that, for the sake of consistency with the method used for averaging the CALIOP DOD within a grid, the single aerosol species re-grid average approach was also used for the MODIS DOD. As shown in Fig. S2, it is very clear that the CALIOP DOD is more consistent with the MODIS DOD than it is with MERRA-2 or DustCOMM, regardless of seasonal and spatial variation. This is especially the case for the dust TCA extending from the TD to the GD and even to the NPO. There are, of course, still significant differences (relative error $>$ 30%, marked in red in Tables S1 and S2) across the three deserts and five transport regions, especially throughout the year in SC. This could be a result of using different sensors and retrieval methods. However, even if uncertainty about the absolute magnitude of the CALIOP DOD estimates cannot be entirely removed, the consistency of the above methods actively advances our understanding of the dust TCA, transport flux, and downstream contribution of desert sources.

4.3. Uncertainties regarding the dust MEE

The dust MEE is closely related to the physical and chemical properties of dust aerosols (Denjean et al., 2020; Ginoux et al., 2012), especially with regard to particle size (Wang et al., 2021a). The accurate seasonal climatology of dust MEE from the DustCOMM dataset was employed in this study. This is significantly better than assuming MEE to be a fixed constant (Huang et al., 2015; Yu et al., 2015a) or a linearly-varying function (Yu et al., 2019a). However, at the same time, vertical changes in the dust particle size and MEE were ignored. It has been proved that the column mean MEE of DustCOMM has a negligible difference (~1%) relative to the MEE measurements. Nonetheless, the DustCOMM dataset is produced based on a constrained model ensemble estimate and there has been a certain amount of uncertainty in the vertical variation in 3-D model simulations (Mahowald et al., 2014; Wang et al., 2020b). To minimize any error relating to this as much as possible, the column mean dust MEE was applied instead of the 3-D dust MEE in our research. Usually, the dust particle size decreases with an increase in altitude, which may cause a higher MEE bias at lower altitudes and a lower MEE bias at higher altitudes. Therefore, we introduce an MEE with one standard deviation to explore the uncertainties caused by the assumption of a vertically unchanged MEE. We give, here, the uncertainties relating to the dust contribution for the sources and the budget in the transport areas caused by having an MEE with one standard deviation. It can be seen in the Table in Fig. 9 that the uncertainty for the source contribution caused by having an MEE with one standard deviation is about 19.90 (29%), 26.17 (18%) and 6.18 (20%) Tg for S1, S2 and S3, respectively. Turning to the transport (see Fig. 13), the absolute (relative) uncertainties for the dust budget are about 7.29 Tg (29%) in NC, 0.3 Tg (10%) in SC, 8.64 Tg (29%) in YS, 6.71 Tg (32%) in JS, and 4.62 Tg (18%) in NPO.

5. Conclusion and discussion

Quantifying the Asian dust cycle from its source to remote regions is essential to understanding the profound impact of dust on the health of human beings and the ecosystem, the terrestrial and oceanic biogeochemical cycles, and the weather and the climate. In this study, we used 3-D dust detection from CALIOP observations between 2007 and 2018 and the seasonal dust MEE climatology from the DustCOMM dataset. The Asian dust DML and transport flux were first estimated and used to validate that the MERRA-2 and DustCOMM datasets. To better characterize the total dust aerosol, the all-day dust extinction was extracted from the natural dust, polluted dust, and dusty marine. The seasonal column-mean MEE from DustCOMM was also used instead of a constant MEE, thereby significantly reducing the uncertainties relating to estimation of the DML and transport flux. The seasonally- and vertically-resolved mass-weighted dust TCA were defined to characterize the variability of the transport routes of Asian dust. Three desert sources and five transport regions were defined to understand the downstream transport contribution from different desert sources and the difference in the dust budgets for terrestrial and oceanic regions. The principal results derived from this study are:

- Although the MERRA-2 reanalysis and DustCOMM datasets have almost the same pattern as the CALIOP-based DOD and DML, both model simulations generally overestimate them for East Asian dust sources and adjacent areas and underestimate them for anthropogenic dust sources (e.g., the North China Plain) and remote regions (e.g., the NPO). This may result from their dependence on the dust size and assumptions made about emission and deposition when setting up the related models.
- There are two typical dust transport routes for Asian dust that affect mainland China and its adjacent seas under the action of the prevailing westerlies. One is the dust aerosols from the deserts in northwest China, together with those from central Asia, which form a heavy transport belt extending from northwest China to the NPO. The other is the dust from South Asia crossing the Hengduan Mountains and the Yunnan-Guizhou Plateau, which mixes with the East Asian dust, before being deposited into the ocean.
- The dust TCA mainly runs across the TD and Hexi Corridor and is controlled by the terrain of northwest inland China. There is an obvious north-south movement over the long-range transport regions across the seasons, which is influenced by the location of the western Pacific subtropical high and Aleutian low. This shifts to the north, reaching up 50°N in the summer, and south, reaching a latitude of at most 35°N in the winter. In addition, with an increase in altitude, the dust TCA and transport direction tend to become a zonal straight line as a result of the strong westerlies.
- The annual transport contribution of the East Asian deserts to mainland China and its adjacent seas is up to 214.28 Tg, accounting for about 88% of the contribution from Asian deserts. This is significantly greater than the contribution from the South Asian deserts (30.43 Tg). The GD is the largest overall contributor to dust transport in Asia, with an annual transport flux of 145.88 Tg, despite it having the smallest DML (~0.21 g m^{-2}). This is largely because the flat terrain and strong northwesterly wind in that region make it easier for the dust aerosol to be transported downstream close to the surface. However, the dust aerosols from TD and ThD can only be transported downstream after having being raised to more than 3 km, because of the elevation of the surrounding terrain.
- The superposition of the natural dust transport and local anthropogenic dust emissions results in a more pronounced dust budget in NC (18.01 Tg) than in SC (3.06 Tg), with the annual budget rate being 21.58 g m^{-2}. The annual budget rate for NC is about 21.58 g m^{-2} larger than that of SC (2.75 g m^{-2}). The dust budget over the ocean may well represent deposition into the ocean, which depends significantly on the dry and wet deposition processes for dust aerosols. The dust deposition rate in YS, JS and NPO is 40.12, 20.41, and 4.01 g m^{-2}, respectively, which decreases as the transport distance increases.

The quantification of the Asian dust cycle in this study fully

encompasses all of the dust components floating in the atmosphere and the seasonal and spatial variation in the dust MEE, thereby giving a more accurate estimation of the Asian dust mass load for future studies. This includes the dust transport flux, the contribution of different desert sources, and even the deposition flux of nutrients into the ocean. The results should assist significantly with providing relevant constraints and improving the simulation ability of the aerosol-related modules in climate models. However, it is should be noted that the dust emissions from different desert sources are difficult to estimate directly because of limitation in the detection methods used by satellites and the frequency of their measurements. Their contribution was therefore indirectly estimated in this study by using the dust transport flux along the dust TCA. It is likely that the East Asian dust contribution is overestimated to some degree, because it includes the transcontinental dust transport contribution of the Central Asian deserts.

There are also some uncertainties associated with assessment of the MEE, the accuracy of the reanalysis of the circulation field and the assumptions made in this study. As mentioned above, dust MEE is negatively correlated with the dust particle effective radius (Wang et al., 2021a). Efforts devoted to retrieving the real-time dust particle effective radius by using multi-wavelength lidar would benefit assessment of the real-time MEE and improve the DML accuracy in future studies. The wind profiles observed by the Aeolus satellite launched in August, 2018 could also be used to improve the accuracy of the atmospheric circulation field provided by the various kinds of reanalysis data (Guo et al., 2021). On that basis, satellite-based remote sensing of the dust cycle could be further strengthened by combining real-time MEE with the observed wind field as an addition to the dust detection capabilities of CALISPO-like in future research. This would provide even deeper and more accurate insights.

Author contributions section

Ying Han: Methodology, Investigation, Software, Visualization, Data analysis, Writing original draft preparation

Tianhe Wang: Conceptualization, Methodology, Visualization, Supervision, Validation, Reviewing and Editing, Project administration

Jingyi Tang: Software, Data curation, Visualization

Chengyun Wang: Data curation, Investigation

Bida Jian: software, Data curation

Jianping Huang: Supervision, Reviewing and Editing, Project administration

Declaration of Competing Interest

The authors declare that they have no known competing financial interests or personal relationships that could have appeared to influence the work reported in this paper.

Acknowledgements

This research is jointly supported by the Second Tibetan Plateau Scientific Expedition and Research Program (STEP, 2019QZKK0602) and the National Natural Science Foundation of China (41775022, 42075174). It is also supported by NASA for making satellite and reanalysis datasets accessible in public. MERRA-2 (https://gmao.gsfc.nasa.gov/reanalysis/MERRA-2/data_access/) is managed from NASA Goddard Earth Sciences Data and Information Services Center (GES DISC). CALIPSO data is from the NASA Langley Research Center Atmospheric Science Data Center (http://eosweb.larc.nasa.gov/). We are also thankful to the efforts made by Dr. Kok, Dr. Adebiyi and their teams in developing the accurate MEE of DustCOMM dataset and making the data available online (http://dustcomm.atmos.ucla.edu/). The authors would like to express their gratitude to EditSprings (https://www.editsprings.cn/) for the expert linguistic services provided.

Appendix A. Supplementary data

Supplementary data to this article can be found online at https://doi.org/10.1016/j.rse.2022.112906.

References

Adebiyi, A.A., Kok, J.F., Wang, Y., Ito, A., Ridley, D.A., Nabat, P., Zhao, C., 2020. Dust Constraints from joint Observational-Modelling-experiMental analysis (DustCOMM): comparison with measurements and model simulations. Atmos. Chem. Phys. 20, 829–863. https://doi.org/10.5194/acp-20-829-2020.

Alizadeh-Choobari, O., Sturman, A., Zawar-Reza, P., 2014. A global satellite view of the seasonal distribution of mineral dust and its correlation with atmospheric circulation. Dyn. Atmos. Oceans 68, 20–34. https://doi.org/10.1016/j.dynatmoce.2014.67.002.

Amiridis, V., Wandinger, U., Marinou, E., Giannakaki, E., Tsekeri, A., Basart, S., Kazadzis, S., Gkikas, A., Taylor, M., Baldasano, J., Ansmann, A., 2013. Optimizing CALIPSO Saharan dust retrievals. Atmos. Chem. Phys. 13, 12089–12106. https://doi.org/10.5194/acp-13-12089-2013.

An, L.C., Che, H.Z., Xue, M., Zhang, T.H., Wang, H., Wang, Y.Q., Zhou, C.H., Zhao, H.J., Gui, K., Zheng, Y., Sun, T.Z., Liang, Y.X., Sun, E.W., Zhang, H.D., Zhang, X.Y., 2018. Temporal and spatial variations in sand and dust storm events in East Asia from 2007 to 2016: Relationships with surface conditions and climate change. Sci. Total Environ. 633, 452–462. https://doi.org/10.1016/j.scitotenv.2018.03.068.

Ansmann, A., Tesche, M., Seifert, P., Gross, S., Freudenthaler, V., Apituley, A., Wilson, K. M., Serikov, I., Linne, H., Heinold, B., Hiebsch, A., Schnell, F., Schmidt, J., Mattis, I., Wandinger, U., Wiegner, M., 2011. Ash and fine-mode particle mass profiles from EARLINET-AERONET observations over central Europe after the eruptions of the Eyjafjallajokull volcano in 2010. J. Geophys. Res. Atmos. 116. https://doi.org/10.1029/2010jd015567.

Ansmann, A., Mamouri, R.E., Hofer, J., Baars, H., Althausen, D., Abdullaev, S.F., 2019. Dust mass, cloud condensation nuclei, and ice-nucleating particle profiling with polarization lidar: updated POLIPHON conversion factors from global AERONET analysis. Atmos. Meas. Tech. 12, 4849–4865. https://doi.org/10.5194/amt-12-4849-2019.

Chen, S., Huang, J., Li, J., Jia, R., Jiang, N., Kang, L., Ma, X., Xie, T., 2017a. Comparison of dust emissions, transport, and deposition between the Taklimakan Desert and Gobi Desert from 2007 to 2011. Sci. China Earth Sci. 60, 1338–1355. https://doi.org/10.1007/s11430-016-9051-0.

Chen, S., Huang, J., Qian, Y., Zhao, C., Kang, L., Yang, B., Wang, Y., Liu, Y., Yuan, T., Wang, T., Ma, X., Zhang, G., 2017b. An overview of mineral dust modeling over East Asia. J. Meteorol. Res. 31, 633–653. https://doi.org/10.1007/s13351-017-6142-2.

Cheng, Y., Dai, T., Li, J., Shi, G., 2020. Measurement Report: Determination of aerosol vertical features on different timescales over East Asia based on CATS aerosol products. Atmos. Chem. Phys. 20, 15307–15322. https://doi.org/10.5194/acp-20-15307-2020.

Denjean, C., Bourrianne, T., Burnet, F., Mallet, M., Maury, N., Colomb, A., Dominutti, P., Brito, J., Dupuy, R., Sellegri, K., Schwarzenboeck, A., Flamant, C., Knippertz, P., 2020. Overview of aerosol optical properties over southern West Africa from DACCIWA aircraft measurements. Atmos. Chem. Phys. 20, 4735–4756. https://doi.org/10.5194/acp-20-4735-2020.

Freudenthaler, V., Esselborn, M., Wiegner, M., Heese, B., Tesche, M., Ansmann, A., MüLler, D., Althausen, D., Wirth, M., Fix, A., Ehret, G., Knippertz, P., Toledano, C., Gasteiger, J., Garhammer, M., Seefeldner, M., 2017. Depolarization ratio profiling at several wavelengths in pure Saharan dust during SAMUM 2006. Tellus Ser. B Chem. Phys. Meteorol. 61, 165–179. https://doi.org/10.1111/j.1600-0889.2008.00396.x.

Fu, P., Huang, J., Li, C., Zhong, S., 2008. The properties of dust aerosol and reducing tendency of the dust storms in northwest China. Atmos. Environ. 42, 5896–5904. https://doi.org/10.1016/j.atmosenv.2008.03.041.

Gelaro, R., McCarty, W., Suarez, M.J., Todling, R., Molod, A., Takacs, L., Randles, C.A., Darmenov, A., Bosilovich, M.G., Reichle, R., Wargan, K., Coy, L., Cullather, R., Draper, C., Akella, S., Buchard, V., Conaty, A., da Silva, A.M., Gu, W., Kim, G.-K., Koster, R., Lucchesi, R., Merkova, D., Nielsen, J.E., Partyka, G., Pawson, S., Putman, W., Rienecker, M., Schubert, S.D., Sienkiewicz, M., Zhao, B., 2017. The Modern-Era Retrospective Analysis for Research and Applications, Version 2 (MERRA-2). J. Clim. 30, 5419–5454. https://doi.org/10.1175/jcli-d-16-0758.1.

Ginoux, P., Deroubaix, A., 2017. Space Observations of Dust in East Asia. Air Pollution in Eastern Asia: An Integrated Perspective. Springer: Cham, pp. 365–383.

Ginoux, P., Clarisse, L., Clerbaux, C., Coheur, P.F., Dubovik, O., Hsu, N.C., Van Damme, M., 2012. Mixing of dust and NH_3 observed globally over anthropogenic dust sources. Atmos. Chem. Phys. 12, 7351–7363. https://doi.org/10.5194/acp-12-7351-2012.

Gross, B., Liu, Z., Winker, D., Omar, A., Vaughan, M., Kar, J., Trepte, C., Hu, Y., Schuster, G., Young, S., Moshary, F., Arend, M., 2016. Aerosol Optical Properties Above Opaque Water Clouds Derived From The Caliop Version 4 Level 1 Data. EPJ Web of Conferences, 119. https://doi.org/10.1051/epjconf/201611904010.

Gueymard, C.A., Yang, D.Z., 2020. Worldwide validation of CAMS and MERRA-2 reanalysis aerosol optical depth products using 15 years of AERONET observations. Atmos. Environ. 225, 18. https://doi.org/10.1016/j.atmosenv.2019.117216.

Guo, J.P., Lou, M.Y., Miao, Y.C., Wang, Y., Zeng, Z.L., Liu, H., He, J., Xu, H., Wang, F., Min, M., Zhai, P.M., 2017. Trans-Pacific transport of dust aerosols from East Asia: Insights gained from multiple observations and modeling. Environ. Pollut. 230, 1030–1039. https://doi.org/10.1016/j.envpol.2017.07.062.

Guo, J., Liu, B., Gong, W., Shi, L., Zhang, Y., Ma, Y., Zhang, J., Chen, T., Bai, K., Stoffelen, A., de Leeuw, G., Xu, X., 2021. Technical note: First comparison of wind observations from ESA's satellite mission Aeolus and ground-based radar wind profiler network of China. Atmos. Chem. Phys. 21, 2945–2958. https://doi.org/10.5194/acp-21-2945-2021.

Hand, J.L., Malm, W.C., 2007. Review of aerosol mass scattering efficiencies from ground-based measurements since 1990. Atmos, J. Geophys. Res., p. 112. https://doi.org/10.1029/2007jd008484

Hayasaka, T., Satake, S., Shimizu, A., Sugimoto, N., Matsui, I., Aoki, K., Muraji, Y., 2007. Vertical distribution and optical properties of aerosols observed over Japan during the Atmospheric Brown Clouds–East Asia Regional Experiment 2005. J. Geophys. Res. Atmos. 112, D22. https://doi.org/10.1029/2006jd008086.

Hofer, J., Ansmann, A., Althausen, D., Engelmann, R., Baars, H., Fomba, K.W., Wandinger, U., Abdullaev, S.F., Makhmudov, A.N., 2020. Optical properties of Central Asian aerosol relevant for spaceborne lidar applications and aerosol typing at 355 and 532 nm. Atmos. Chem. Phys. 20, 9265–9280. https://doi.org/10.5194/acp-20-9265-2020.

Hsu, S.-C., Liu, S.C., Arimoto, R., Liu, T.-H., Huang, Y.-T., Tsai, F., Lin, F.-J., Kao, S.-J., 2009. Dust deposition to the East China Sea and its biogeochemical implications. J. Geophys. Res. Atmos. 114. https://doi.org/10.1029/2008jd011223.

Hu, Y., Vaughan, M., Liu, Z., Powell, K., Rodier, S., 2007. Retrieving optical depths and lidar ratios for transparent layers above opaque water clouds from CALIPSO lidar measurements. IEEE Geosci. Remote Sens. Lett. 4, 523–526. https://doi.org/10.1109/lgrs.2007.901085.

Hu, Q., Wang, H., Goloub, P., Li, Z., Veselovskii, I., Podvin, T., Li, K., Korenskiy, M., 2020. The characterization of Taklamakan dust properties using a multiwavelength Raman polarization lidar in Kashi. China. Atmos. Chem. Phys. 20, 13817–13834. https://doi.org/10.5194/acp-20-13817-2020.

Huang, J., Ge, J., Weng, F., 2007. Detection of Asia dust storms using multisensor satellite measurements. Remote Sens. Environ. 110, 186–191. https://doi.org/10.1016/j.rse.2007.02.022.

Huang, J., Minnis, P., Chen, B., Huang, Z., Liu, Z., Zhao, Q., Yi, Y., Ayers, J.K., 2008. Long-range transport and vertical structure of Asian dust from CALIPSO and surface measurements during PACDEX. J. Geophys. Res. Atmos. 113. https://doi.org/10.1029/2008jd010620.

Huang, J., Wang, T., Wang, W., Li, Z., Yan, H., 2014. Climate effects of dust aerosols over East Asian arid and semiarid regions. J. Geophys. Res. Atmos. 119, 398–416. https://doi.org/10.1002/2014jd021796.

Huang, J.P., Liu, J.J., Chen, B., Nasiri, S.L., 2015. Detection of anthropogenic dust using CALIPSO lidar measurements. Atmos. Chem. Phys. 15, 11653–11665. https://doi.org/10.5194/acp-15-11653-2015.

Huneeus, N., Schulz, M., Balkanski, Y., Griesfeller, J., Prospero, J., Kinne, S., Bauer, S., Boucher, O., Chin, M., Dentener, F., Diehl, T., Easter, R., Fillmore, D., Ghan, S., Ginoux, P., Grini, A., Horowitz, L., Koch, D., Krol, M.C., Landing, W., Liu, X., Mahowald, N., Miller, R., Morcrette, J.J., Myhre, G., Penner, J., Perlwitz, J., Stier, P., Takemura, T., Zender, C.S., 2011. Global dust model intercomparison in AeroCom phase I. Atmos. Chem. Phys. 11, 7781–7816. https://doi.org/10.5194/acp-11-7781-2011.

Jickells, T.D., An, Z.S., Andersen, K.K., Baker, A.R., Bergametti, G., Brooks, N., Cao, J.J., Boyd, P.W., Duce, R.A., Hunter, K.A., Kawahata, H., Kubilay, N., laRoche, J., Liss, P. S., Mahowald, N., Prospero, J.M., Ridgwell, A.J., Tegen, I., Torres, R., 2005. Global iron connections between desert dust, ocean biogeochemistry, and climate. Science. 308, 67–71. https://doi.org/10.1126/science.1105959.

Kaufman, Y.J., Tanre, D., Boucher, O., 2002. A satellite view of aerosols in the climate system. Nature. 419, 215–223. https://doi.org/10.1038/nature01091.

Kaufman, Y.J., Koren, I., Remer, L.A., Tanre, D., Ginoux, P., Fan, S., 2005. Dust transport and deposition observed from the Terra-Moderate Resolution Imaging Spectroradiometer (MODIS) spacecraft over the Atlantic ocean. J. Geophys. Res. Atmos. 110. https://doi.org/10.1029/2003jd004436.

Kim, S.-W., Yoon, S.-C., Kim, J., Kang, J.-Y., Sugimoto, N., 2010. Asian dust event observed in Seoul, Korea, during 29-31 May 2008: Analysis of transport and vertical distribution of dust particles from lidar and surface measurements. Sci. Total Environ. 408, 1707–1718. https://doi.org/10.1016/j.scitotenv.2009.12.018.

Kim, M.-H., Omar, A.H., Tackett, J.L., Vaughan, M.A., Winker, D.M., Trepte, C.R., Hu, Y., Liu, Z., Poole, L.R., Pitts, M.C., Kar, J., Magill, B.E., 2018. The CALIPSO version 4 automated aerosol classification and lidar ratio selection algorithm. Atmos. Meas. Tech. 11, 6107–6135. https://doi.org/10.5194/amt-11-6107-2018.

Kim, D., Chin, M., Yu, H.B., Pan, X.H., Bian, H.S., Tan, Q., Kahn, R.A., Tsigaridis, K., Bauer, S.E., Takemura, T., Pozzoli, L., Bellouin, N., Schulz, M., 2019. Asian and trans-pacific dust: A multimodel and multiremote Sensing observation analysis. J. Geophys. Res. Atmos. 124, 13534–13559. https://doi.org/10.1029/2019jd030822.

Klose, M., Shao, Y., Li, X., Zhang, H., Ishizuka, M., Mikami, M., Leys, J.F., 2014. Further development of a parameterization for convective turbulent dust emission and evaluation based on field observations. J. Geophys. Res. Atmos. 119. https://doi.org/10.1002/2014jd021688.

Kok, J.F., Ridley, D.A., Zhou, Q., Miller, R.L., Zhao, C., Heald, C.L., Ward, D.S., Albani, S., Haustein, K., 2017. Smaller desert dust cooling effect estimated from analysis of dust size and abundance. Nat. Geosci. 10, 274–278. https://doi.org/10.1038/ngeo2912.

Kudo, R., Nishizawa, T., Aoyagi, T., 2016. Vertical profiles of aerosol optical properties and the solar heating rate estimated by combining sky radiometer and lidar measurements. Atmos. Meas. Tech. 9, 3223–3243. https://doi.org/10.5194/amt-9-3223-2016.

Lakshmi, N.B., Nair, V.S., Babu, S.S., 2021. Assessment of the vertical distribution of speciated aerosol absorption over South Asia using spaceborne LIDAR and ground-based observations. Remote Sens. Environ. 253. https://doi.org/10.1016/j.rse.2020.112164.

Lau, K.M., Kim, M.K., Kim, K.M., 2006. Asian summer monsoon anomalies induced by aerosol direct forcing: the role of the Tibetan Plateau. Clim. Dyn. 26, 855–864. https://doi.org/10.1007/s00382-006-0114-z.

Lau, W.K.M., Sang, J., Kim, M.K., Kim, K.M., Koster, R.D., Yasunari, T.J., 2018. Impacts of Snow Darkening by Deposition of Light-Absorbing Aerosols on Hydroclimate of Eurasia During Boreal Spring and Summer. J. Geophys. Res. Atmos. 123, 8441–8461. https://doi.org/10.1029/2018jd028557.

Liu, Y., Sato, Y., Jia, R., Xie, Y., Huang, J., Nakajima, T., 2015. Modeling study on the transport of summer dust and anthropogenic aerosols over the Tibetan Plateau. Atmos. Chem. Phys. 15, 12581–12594. https://doi.org/10.5194/acp-15-12581-2015.

Liu, Z., Kar, J., Zeng, S., Tackett, J., Vaughan, M., Avery, M., Pelon, J., Getzewich, B., Lee, K.-P., Magill, B., Omar, A., Lucker, P., Trepte, C., Winker, D., 2019. Discriminating between clouds and aerosols in the CALIOP version 4.1 data products. Atmos. Meas. Tech. 12, 703–734. https://doi.org/10.5194/amt-12-703-2019.

Luo, T., Wang, Z., Zhang, D., Liu, X., Wang, Y., Yuan, R., 2015. Global dust distribution from improved thin dust layer detection using A-train satellite lidar observations. Geophys. Res. Lett. 42, 620–628. https://doi.org/10.1002/2014gl062111.

Mahowald, N., Albani, S., Kok, J.F., Engelstaeder, S., Scanza, R., Ward, D.S., Flanner, M. G., 2014. The size distribution of desert dust aerosols and its impact on the Earth system. Aeolian Res. 15, 53–71. https://doi.org/10.1016/j.aeolia.2013.09.002.

Maki, T., Lee, K.C., Pointing, S.B., Watanabe, K., Aoki, K., Archer, S.D.J., Lacap-Bugler, D.C., Ishikawa, A., 2021. Desert and anthropogenic mixing dust deposition influences microbial communities in surface waters of the western Pacific Ocean. Sci. Total Environ. 791, 148026. https://doi.org/10.1016/j.scitotenv.2021.148026.

Mamouri, R.E., Ansmann, A., 2014. Fine and coarse dust separation with polarization lidar. Atmos. Meas. Tech. 7, 3717–3735. https://doi.org/10.5194/amt-7-3717-2014.

Meng, L., Gao, H.W., Yu, Y., Yao, X.H., Gao, Y., Zhang, C., Fan, L., 2017. A new approach developed to study variability in North African dust transport routes over the Atlantic during 2001–2015. Geophys. Res. Lett. 44 https://doi.org/10.1002/2017gl074478.

Müller, D., Weinzierl, B., Petzold, A., Kandler, K., Ansmann, A., Müller, T., Tesche, M., Freudenthaler, V., Esselborn, M., Heese, B., Althausen, D., Schladitz, A., Otto, S., Knippertz, P., 2010. Mineral dust observed with AERONET Sun photometer, Raman lidar, and in situ instruments during SAMUM 2006: Shape-independent particle properties. J. Geophys. Res. Atmos. 115. https://doi.org/10.1029/2009jd012520.

Naeger, A.R., Gupta, P., Zavodsky, B.T., McGrath, K.M., 2016. Monitoring and tracking the trans-Pacific transport of aerosols using multi-satellite aerosol optical depth composites. Atmos. Meas. Tech. 9, 2463–2482. https://doi.org/10.5194/amt-9-2463-2016.

Omar, A.H., Winker, D.M., Kittaka, C., Vaughan, M.A., Liu, Z., Hu, Y., Trepte, C.R., Rogers, R.R., Ferrare, R.A., Lee, K.-P., Kuehn, R.E., Hostetler, C.A., 2009a. The CALIPSO Automated Aerosol Classification and Lidar Ratio Selection Algorithm. J. Atmos. Ocean. Technol. 26, 1994–2014. https://doi.org/10.1175/2009jtecha1231.1.

Omar, A.H., Winker, D.M., Kittaka, C., Vaughan, M.A., Liu, Z.Y., Hu, Y.X., Trepte, C.R., Rogers, R.R., Ferrare, R.A., Lee, K.P., Kuehn, R.E., Hostetler, C.A., 2009b. The CALIPSO Automated Aerosol Classification and Lidar Ratio Selection Algorithm. J. Atmos. Ocean. Technol. 26, 1994–2014. https://doi.org/10.1175/2009jtecha1231.1.

Omar, A.H., Winker, D.M., Tackett, J.L., Giles, D.M., Kar, J., Liu, Z., Vaughan, M.A., Powell, K.A., Trepte, C.R., 2013. CALIOP and AERONET aerosol optical depth comparisons: One size fits none. J. Geophys. Res. Atmos. 118, 4748–4766. https://doi.org/10.1002/jgrd.50330.

Pan, H.L., Huo, W., Wang, M.Z., Zhang, J.T., Meng, L., Kumar, K.R., Devi, N., 2020. Insight into the climatology of different sand-dust aerosol types over the Taklimakan Desert based on the observations from radiosonde and A-train satellites. Atmos. Environ. 238, 17. https://doi.org/10.1016/j.atmosenv.2020.117705.

Paulot, F., Paynter, D., Ginoux, P., Naik, V., Horowitz, L.W., 2018. Changes in the aerosol direct radiative forcing from 2001 to 2015: observational constraints and regional mechanisms. Atmos. Chem. Phys. 18, 13265–13281. https://doi.org/10.5194/acp-18-13265-2018.

Proestakis, E., Amiridis, V., Marinou, E., Georgoulias, A.K., Solomos, S., Kazadzis, S., Chimot, J., Che, H.Z., Alexandri, G., Binietoglou, I., Daskalopoulou, V., Kourtidis, K. A., de Leeuw, G., Ronald, J.V., 2018. Nine-year spatial and temporal evolution of desert dust aerosols over South and East Asia as revealed by CALIOP. Atmos. Chem. Phys. 18, 1337–1362. https://doi.org/10.5194/acp-18-1337-2018.

Prospero, J.M., Barkley, A.E., Gaston, C.J., Gatineau, A., Campos y Sansano, A., Panechou, K., 2020. Characterizing and Quantifying African Dust Transport and Deposition to South America: Implications for the Phosphorus Budget in the Amazon Basin. Glob. Biogeochem. Cycles 34. https://doi.org/10.1029/2020gb006536.

Randles, C.A., da Silva, A.M., Buchard, V., Colarco, P.R., Darmenov, A., Govindaraju, R., Smirnov, A., Holben, B., Ferrare, R., Hair, J., Shinozuka, Y., Flynn, C.J., 2017. The MERRA-2 aerosol reanalysis, 1980 onward. Part I: system description and data assimilation evaluation. J. Clim. 30, 6823–6850. https://doi.org/10.1175/Jcli-D-16-0609.1.

Schepanski, K., 2018. Transport of Mineral Dust and Its Impact on Climate. Geosci. 8 https://doi.org/10.3390/geosciences8050151.

Schuerger, A.C., Smith, D.J., Griffin, D.W., Jaffe, D.A., Wawrik, B., Burrows, S.M., Christner, B.C., Gonzalez-Martin, C., Lipp, E.K., Schmale, D.G., Yu, H.B., 2018. Science questions and knowledge gaps to study microbial transport and survival in Asian and African dust plumes reaching North America. Aerobiologia. 34, 425–435. https://doi.org/10.1007/s10453-018-9541-7.

Schulz, M., Prospero, J.M., Baker, A.R., Dentener, F., Ickes, L., Liss, P.S., Mahowald, N. M., Nickovic, S., Garcia-Pando, C.P., Rodriguez, S., Sarin, M., Tegen, I., Duce, R.A., 2012. Atmospheric transport and deposition of mineral dust to the ocean: implications for research needs. Environ. Sci. Technol. 46, 10390–10404. https://doi.org/10.1021/es300073u.

Shao, Y., Dong, C.H., 2006. A review on East Asian dust storm climate, modelling and monitoring. Glob. Planet. Chang. 52, 1–22. https://doi.org/10.1016/j.gloplacha.2006.02.011.

Shao, Y., Wyrwoll, K.-H., Chappell, A., Huang, J., Lin, Z., McTainsh, G.H., Mikami, M., Tanaka, T.Y., Wang, X., Yoon, S., 2011. Dust cycle: An emerging core theme in Earth system science. Aeolian Res. 2, 181–204. https://doi.org/10.1016/j.aeolia.2011.02.001.

Shen, Z., Cao, J., Arimoto, R., Han, Y., Zhu, C., Tian, J., Liu, S., 2010. Chemical Characteristics of Fine Particles (PM1) from Xi'an. China. Aerosol Sci. Technol. 44, 461–472. https://doi.org/10.1080/02786821003738908.

Shi, J.-H., Gao, H.-W., Zhang, J., Tan, S.-C., Ren, J.-L., Liu, C.-G., Liu, Y., Yao, X., 2012. Examination of causative link between a spring bloom and dry/wet deposition of Asian dust in the Yellow Sea. China. J. Geophys. Res.: Atmos. 117. https://doi.org/10.1029/2012jd017983.

Shi, L.M., Zhang, J.H., Yao, F.M., Zhang, D., Guo, H.D., 2020. Temporal variation of dust emissions in dust sources over Central Asia in recent decades and the climate linkages. Atmos. Environ. 222, 15. https://doi.org/10.1016/j.atmosenv.2019.117176.

Sicard, P., Crippa, P., De Marco, A., Castruccio, S., Giani, P., Cuesta, J., Paoletti, E., Feng, Z., Anav, A., 2021. High spatial resolution WRF-Chem model over Asia: Physics and chemistry evaluation. Atmos. Environ. 244 https://doi.org/10.1016/j.atmosenv.2020.118004.

Sivan, C., Rakesh, V., Abhilash, S., Mohanakumar, K., 2021. Evaluation of global reanalysis winds and high-resolution regional model outputs with the 205 MHz stratosphere-troposphere wind profiler radar observations. Q. J. R. Meteorol. Soc. 18 https://doi.org/10.1002/qj.4041.

Song, Q., Zhang, Z., Yu, H., Ginoux, P., Shen, J., 2021. Global dust optical depth climatology derived from CALIOP and MODIS aerosol retrievals on decadal timescales: regional and interannual variability. Atmos. Chem. Phys. 21, 13369–13395. https://doi.org/10.5194/acp-21-13369-2021.

Sugimoto, N., Huang, Z.W., 2014. Lidar methods for observing mineral dust. J. Meteorol. Res. 28, 173–184. https://doi.org/10.1007/s13351-014-3068-9.

Sugimoto, N., Matsui, I., Shimizu, A., Uno, I., Asai, K., Endoh, T., Nakajima, T., 2002. Observation of dust and anthropogenic aerosol plumes in the Northwest Pacific with a two-wavelength polarization lidar on board the research vessel Mirai. Geophys. Res. Lett. 29 https://doi.org/10.1029/2002gl015112, 7-1-7-4.

Sugimoto, N., Jin, Y., Shimizu, A., Nishizawa, T., Yumimoto, K., 2019. Transport of Mineral Dust from Africa and Middle East to East Asia Observed with the Lidar Network (AD-Net). Sola. 15, 257–261. https://doi.org/10.2151/sola.2019-046.

Sun, H., Liu, X.D., Wang, A.Q., 2020. Seasonal and interannual variations of atmospheric dust aerosols in mid and low latitudes of Asia - A comparative study. Atmos. Res. 244, 11. https://doi.org/10.1016/j.atmosres.2020.105036.

Tesche, M., Wandinger, U., Ansmann, A., Althausen, D., Mueller, D., Omar, A.H., 2013. Ground-based validation of CALIPSO observations of dust and smoke in the Cape Verde region. J. Geophys. Res. Atmos. 118, 2889–2902. https://doi.org/10.1002/jgrd.50248.

Toth, T.D., Zhang, J.L., Campbell, J.R., Reid, J.S., Vaughan, M.A., 2016. Temporal variability of aerosol optical thickness vertical distribution observed from CALIOP. J. Geophys. Res. Atmos. 121, 9117–9139. https://doi.org/10.1002/2015jd024668.

Uno, I., Wang, Z., Chiba, M., Chun, Y.S., Gong, S.L., Hara, Y., Jung, E., Lee, S.S., Liu, M., Mikami, M., Music, S., Nickovic, S., Satake, S., Shao, Y., Song, Z., Sugimoto, N., Tanaka, T., Westphal, D.L., 2006. Dust model intercomparison (DMIP) study over Asia: Overview. J. Geophys. Res. Atmos. 111. https://doi.org/10.1029/2005jd006575.

Uno, I., Eguchi, K., Yumimoto, K., Takemura, T., Shimizu, A., Uematsu, M., Liu, Z., Wang, Z., Hara, Y., Sugimoto, N., 2009. Asian dust transported one full circuit around the globe. Nat. Geosci. 2, 557–560. https://doi.org/10.1038/ngeo583.

Uno, I., Eguchi, K., Yumimoto, K., Liu, Z., Hara, Y., Sugimoto, N., Shimizu, A., Takemura, T., 2011. Large Asian dust layers continuously reached North America in April 2010. Atmos. Chem. Phys. 11, 7333–7341. https://doi.org/10.5194/acp-11-7333-2011.

Usha, K.H., Nair, V.S., Babu, S.S., 2021. Effect of aerosol-induced snow darkening on the direct radiative effect of aerosols over the Himalayan region. Environ. Res. Lett. 16 https://doi.org/10.1088/1748-9326/abf190.

Wandinger, U., Tesche, M., Seifert, P., Ansmann, A., Müller, D., Althausen, D., 2010. Size matters: Influence of multiple scattering on CALIPSO light-extinction profiling in desert dust. Geophys. Res. Lett. 37 https://doi.org/10.1029/2010gl042815 n/a-n/a.

Wang, S.-H., Hsu, N.C., Tsay, S.-C., Lin, N.-H., Sayer, A.M., Huang, S.-J., Lau, W.K.M., 2012. Can Asian dust trigger phytoplankton blooms in the oligotrophic northern South China Sea? Geophys. Res. Lett. 39 https://doi.org/10.1029/2011gl050415.

Wang, T., Han, Y., Huang, J., Sun, M., Jian, B., Huang, Z., Yan, H., 2020a. Climatology of Dust-Forced Radiative Heating Over the Tibetan Plateau and Its Surroundings. J. Geophys. Res. Atmos. 125. https://doi.org/10.1029/2020jd032942.

Wang, Y., Zheng, X., Dong, X., Xi, B., Wu, P., Logan, T., Yung, Y.L., 2020b. Impacts of long-range transport of aerosols on marine-boundary-layer clouds in the eastern North Atlantic. Atmos. Chem. Phys. 20, 14741–14755. https://doi.org/10.5194/acp-20-14741-2020.

Wang, T., Han, Y., Hua, W., Tang, J., Huang, J., T, Z., Huang, Z., J, B., Xie, H., 2021a. Profiling Dust Mass Concentration in Northwest China Using a Joint Lidar and Sun-Photometer Setting. Remote Sens. 13, 1099. https://doi.org/10.3390/rs13061099.

Wang, T.H., Tang, J.Y., Sun, M.X., Liu, X.W., Huang, Y.X., Huang, J.P., Han, Y., Cheng, Y. F., Huang, Z.W., Li, J.M., 2021b. Identifying a transport mechanism of dust aerosols over South Asia to the Tibetan Plateau: A case study. Sci. Total Environ. 758 https://doi.org/10.1016/j.scitotenv.2020.143714.

Winker, D.M., Vaughan, M.A., Omar, A., Hu, Y., Powell, K.A., Liu, Z., Hunt, W.H., Young, S.A., 2009. Overview of the CALIPSO Mission and CALIOP Data Processing Algorithms. J. Atmos. Ocean. Technol. 26, 2310–2323. https://doi.org/10.1175/2009jtecha1281.1.

Winker, D.M., Tackett, J.L., Getzewich, B.J., Liu, Z., Vaughan, M.A., Rogers, R.R., 2013. The global 3-D distribution of tropospheric aerosols as characterized by CALIOP. Atmos. Chem. Phys. 13, 3345–3361. https://doi.org/10.5194/acp-13-3345-2013.

Wu, M., Liu, X., Yu, H., Wang, H., Shi, Y., Yang, K., Darmenov, A., Wu, C., Wang, Z., Luo, T., Feng, Y., Ke, Z., 2020. Understanding processes that control dust spatial distributions with global climate models and satellite observations. Atmos. Chem. Phys. 20, 13835–13855. https://doi.org/10.5194/acp-20-13835-2020.

Xu, C., Ma, Y., Yang, K., You, C., 2018. Tibetan Plateau Impacts on Global Dust Transport in the Upper Troposphere. J. Clim. 31, 4745–4756. https://doi.org/10.1175/Jcli-D-17-0313.1.

Yu, H.B., Remer, L.A., Chin, M., Bian, H.S., Tan, Q., Yuan, T.L., Zhang, Y., 2012. Aerosols from Overseas Rival Domestic Emissions over North America. Science. 337, 566–569. https://doi.org/10.1126/science.1217576.

Yu, H., Chin, M., Bian, H., Yuan, T., Prospero, J.M., Omar, A.H., Remer, L.A., Winker, D. M., Yang, Y., Zhang, Y., Zhang, Z., 2015a. Quantification of trans-Atlantic dust transport from seven-year (2007–2013) record of CALIPSO lidar measurements. Remote Sens. Environ. 159, 232–249. https://doi.org/10.1016/j.rse.2014.12.010.

Yu, H.B., Chin, M., Yuan, T.L., Bian, H.S., Remer, L.A., Prospero, J.M., Omar, A., Winker, D., Yang, Y.K., Zhang, Y., Zhang, Z.B., Zhao, C., 2015b. The fertilizing role of African dust in the Amazon rainforest: A first multiyear assessment based on data from Cloud-Aerosol Lidar and Infrared Pathfinder Satellite Observations. Geophys. Res. Lett. 42, 1984–1991. https://doi.org/10.1002/2015gl063040.

Yu, H., Tan, Q., Chin, M., Remer, L.A., Kahn, R.A., Bian, H., Kim, D., Zhang, Z., Yuan, T., Omar, A.H., Winker, D.M., Levy, R.C., Kalashnikova, O., Crepeau, L., Capelle, V., Chédin, A., 2019a. Estimates of African Dust Deposition Along the Trans-Atlantic Transit Using the Decadelong Record of Aerosol Measurements from CALIOP, MODIS, MISR, and IASI. J. Geophys. Res. Atmos. 124, 7975–7996. https://doi.org/10.1029/2019jd030574.

Yu, Y., Kalashnikova, O.V., Garay, M.J., Notaro, M., 2019b. Climatology of Asian dust activation and transport potential based on MISR satellite observations and trajectory analysis. Atmos. Chem. Phys. 19, 363–378. https://doi.org/10.5194/acp-19-363-2019.

Yu, H.B., Yang, Y., Wang, H.L., Tan, Q., Chin, M., Levy, R.C., Remer, L.A., Smith, S.J., Yuan, T.L., Shi, Y.X., 2020. Interannual variability and trends of combustion aerosol and dust in major continental outflows revealed by MODIS retrievals and CAM5 simulations during 2003-2017. Atmos. Chem. Phys. 20, 139–161. https://doi.org/10.5194/acp-20-139-2020.

Zhang, X.Y., Arimoto, R., An, Z.S., 1997. Dust emission from Chinese desert sources linked to variations in atmospheric circulation. J. Geophys. Res. Atmos. 102, 28041–28047. https://doi.org/10.1029/97JD02300.

Zhang, X.Y., Gong, S.L., Shen, Z.X., Mei, F.M., Xi, X.X., Liu, L.C., Zhou, Z.J., Wang, D., Wang, Y.Q., Cheng, Y., 2003a. Characterization of soil dust aerosol in China and its transport and distribution during 2001 ACE-Asia: 1. Network observations. J. Geophys. Res. Atmos. 108, 4262. https://doi.org/10.1029/2002jd002632.

Zhang, X.Y., Gong, S.L., Zhao, T.L., Arimoto, R., Wang, Y.Q., Zhou, Z.J., 2003b. Sources of Asian dust and role of climate change versus desertification in Asian dust emission. Geophys. Res. Lett. 30 https://doi.org/10.1029/2003GL018206.

Zhang, D., Iwasaka, Y., Shi, G., Zang, J., Hu, M., Li, C., 2005. Separated status of the natural dust plume and polluted air masses in an Asian dust storm event at coastal areas of China. J. Geophys. Res. Atmos. 110, D06302 https://doi.org/10.1029/2004jd005305.

Zhang, C., He, J., Yao, X., Mu, Y., Guo, X., Ding, X., Yu, Y., Shi, J., Gao, H., 2020. Dynamics of phytoplankton and nutrient uptake following dust additions in the northwest Pacific. Sci. Total Environ. 739 https://doi.org/10.1016/j.scitotenv.2020.139999.

Zhou, C.L., Yang, F., Mamtimin, A., Huo, W., Liu, X.C., He, Q., Zhang, J.T., Yang, X.H., 2020a. Wind erosion events at different wind speed levels in the Tarim Basin. Geomorphology. 369 https://doi.org/10.1016/j.geomorph.2020.107386.

Zhou, Y., Xiao, H., Guan, H., Zheng, N., Zhang, Z., Tian, J., Qu, L., Zhao, J., Xiao, H., 2020b. Chemical composition and seasonal variations of PM2.5 in an urban environment in Kunming, SW China: Importance of prevailing westerlies in cold season. Atmos. Environ. 237 https://doi.org/10.1016/j.atmosenv.2020.117704.